

XLES Part II: From Extended Large Eddy Simulation to ODTLES

Christoph Glawe^{a,c}, Heiko Schmidt^a, Alan R. Kerstein^b, Rupert Klein^c

^a*BTU Cottbus-Senftenberg, Siemens-Halske-Ring 14, 03046 Cottbus, Germany*

^b*72 Lomitas Road, Danville, CA 94526, USA*

^c*FU Berlin, Arnimallee 6, 14195 Berlin, Germany*

Abstract

In turbulence research and flow applications, turbulence models like RaNS (Reynolds averaged Navier-Stokes) models and LES (Large Eddy Simulation) are used. Both models filter the governing flow equations. Thus a scale separation approach is introduced for modeling purposes with the large scales simulated using a numerical scheme while smaller scales are assumed to be less important and might be modeled more or less easily. Unfortunately small scales are frequently of big importance, e.g. in reactive flows, wall bounded flows, or flows with significant Prandtl or Schmidt number effects. Recent alternatives to these standard models are the class of models based on the one-dimensional turbulence (ODT) idea, like ODTLES. The ability of ODT to capture highly turbulent flows (recently up to $Re_\tau = 6 \times 10^5$) allows ODTLES to realize 3D resolutions basically independent of the turbulent intensity. In two papers we provide a formal theory and application of an innovative modeling strategy for highly turbulent flows in domains of moderate complexity: In part I (see Glawe et al. (2015)) a new general filtering approach, called XLES (extended LES), is introduced. Contrary to LES, XLES is based on 2D filtering of the governing equations, whereby additional small scale terms are interpreted numerically. In this work a new ansatz for the ODTLES model is introduced as one special approach in the XLES family of models by incorporating the ODT model into XLES. The ODT model introduces microstructures not captured by the XLES filtered equations. To illustrate the ODTLES model capabilities, turbulent channel and duct flows up to friction Reynolds number $Re_\tau = 10000$ are studied.

Email address: Christoph.Glawe@protonmail.com (Christoph Glawe)

Keywords:

Extended Large Eddy Simulations (XLES), Large Eddy Simulation, One-Dimensional Turbulence, Stochastic Turbulence Modeling, Channel Flow

1. Introduction

In fluid mechanics an increasing number of scientific and industrial problems are amenable to computer simulations due to growing computational power. Realistic problems, e.g. in engineering and meteorology, require the application of turbulence models to reduce the computational effort. For an overview of turbulence properties and model approaches see e.g. Pope (2000).

Large Eddy Simulation (LES, see e.g. Sagaut (2006)) is widely used in fundamental research and increasingly in industrial applications. In LES, 3D spatially filtered equations, containing large scale properties down to the inertial range of the turbulent cascade, are solved numerically. The effect of the unresolved scales is modeled, e.g. by an eddy viscosity model (see e.g. Germano et al. (1991)).

In the area of reactive and wall bounded flows, especially with significant Prandtl or Schmidt number effects, small scale properties are very important, but not adequately represented by simple sub-grid models.

Recent alternative models including the one-dimensional turbulence (ODT) model (see e.g. Kerstein (1999) and Kerstein et al. (2001)) describe the 3D turbulence in a 1D sub-domain, whereby the numerical representation of molecular diffusive effects becomes computationally feasible also in highly turbulent flows. E.g. Meiselbach (2015b) presents wall bounded flows up to $Re_\tau = 6 \times 10^5$. This model appropriately describes individual flows involving one characteristic and predominant direction including the full turbulent cascade, which is valid inter alia in important problems within the research fields of fundamental combustion or atmospheric science.

In ODTLES the ODT model represents the microstructure terms (often called sub-grid model SGM), whereby the macrostructural model has to fulfill special requirements, which are satisfied by the extended Large Eddy Simulation (XLES) ansatz, introduced in part I (Glawe et al. (2015)): Three 2D filtered and coupled sets of equations are solved and discretized by three XLES-grids. Each set of equations corresponds to one predominant Cartesian direction. The XLES unresolved sub-grid scale (SGS) terms are connected to

the ODT advancement, where ODT is interpreted in terms of Navier-Stokes advection, rather than a stochastic (Monte-Carlo like) model. This so called ODTLES model (2D filtered XLES equations with ODT microstructure modeling) combines the diffusive and advective small-scale effects computed by ODT with the ability to discretize 3D domains within a macrostructural model. Because ODT is able to describe the full turbulent spectrum in a 1D sub-domain, only 3D effects not represented by ODT (e.g. the domain, secondary instabilities, ...) need to be resolved in 3D by XLES.

Here we distinguish between the expressions XLES to describe the XLES approach including an approximation or model for arising microscale terms, ODTLES if these terms are in particular described by ODT and XLES-U (XLES unclosed), if microscale terms are neglected.

A previous version of ODTLES, introduced and examined by Schmidt et al. (2008), Gonzalez-Juez et al. (2011), and Glawe et al. (2013), solves weakly coupled XLES equations that generate inconsistent 3D large scale velocity fields on the three XLES-grids. This introduces certain oscillations of the root mean square velocity (reported by Gonzalez-Juez et al. (2011)) but no further major qualitative change in results.

Though primarily intended to explain ODTLES to the LES community, XLES also gives new insights into ODTLES (e.g. allows to represent scalar properties by multiple XLES-grids consistently) and moreover is a novel autonomous modeling strategy because the ansatz is very general and not limited to one-dimensional models like ODT.

There are other approaches like LES-ODT (e.g. by Cao and Echehki (2008)), LES-LEM (by Menon and Kerstein (2011)), and LEM3D (e.g. by Sannan et al. (2013)) connecting 1D turbulence models and 3D computations. These approaches are not considered in detail in this work.

In this work the ODT model is briefly introduced in section 2 and the XLES approach, introduced in detail in part I (Glawe et al. (2015)), is summarized in section 3. Section 4 introduces the ODT model as closure for XLES. The time advancement cycle of the ODT closed XLES model (ODTLES) in section 5 summarizes the model derivation, followed by channel and duct flow results in section 6, comparative estimations of the computational costs in section 7, and final conclusions in section 8.

In accord with part I (Glawe et al. (2015)) we assume the flow to be described by the incompressible Navier-Stokes equations for a Newtonian fluid with constant kinematic viscosity (ν) and constant density (for simplicity we assume $\rho_0 = 1$).

Note that in this work no Einstein summation convention is used.

2. One-Dimensional Turbulence Model (ODT)

The ODT model describes the dynamics of a three dimensional turbulent flow within a one-dimensional sub-domain, including fully resolved molecular diffusion. Thus ODT is a dynamical model, able to describe e.g. the turbulent channel flow including high order flow statistics with high accuracy (see Appendix A).

ODT stand-alone is able to compute meaningful results, even with one velocity component (see Kerstein (1999)). Nevertheless to capture anisotropic flow behavior and especially as a closure within a 3D approach, two or three velocity components are advantageous.

In wall-bounded flows (especially in turbulent channel flows) described by ODT with three velocity components, the wall-normal and the spanwise velocities are identical, so two-component ODT captures similar statistical flow properties. (Note that ODT results in Appendix A are computed with 2 velocity components).

In this section the ODT time advancement is described briefly. Here we introduce ODT including 2 velocity components. This ODT model is a modification of the ODT vector formulation by Kerstein et al. (2001) including 3 velocity components.

ODT emulates the time evolution of a turbulent 3D fluid in a 1D subspace, which is oriented in the Cartesian x_k -direction. The 2 ODT velocity components $u_{k,i}$ (with $k \neq i$) are oriented orthogonally to the x_k -direction. The time evolution of a velocity field $u_{k,i}$ in this 1D subspace is described by:

$$(\partial_t u_{k,i} + \mathcal{D}_{\text{ODT}_k}(u_{k,i}) + e_{k,i}(u_{k,i}; x_0, l)) = 0 \text{ with } k, i = \{1, 2, 3\} \wedge i \neq k \quad (1)$$

with the ODT diffusion term $\mathcal{D}_{\text{ODT}_k}(u_{k,i}) = -\nu \partial_{x_k}^2 u_{k,i}$ which is numerically approximated by an implicit Euler scheme in time and a central difference scheme in space. The index notation resembles the XLES index notation used in the following sections with the velocity $u_{k,i}$ oriented in the x_i -direction within a 1D sub-space oriented in the x_k -direction ($i \neq k$).

The term $e_{k,i}(u_{k,i}; x_0, l)$ is an instantaneous eddy function affecting $u_{k,i}$ within the eddy range $x_k \in [x_0, x_0 + l]$. The maximum eddy length l^{max} is enforced, hence $l \leq l^{\text{max}}$. The eddy function $e_{k,i}$ is introduced to represent a

stochastic procedure that emulates turbulent advection:

$$e_{k,i} : u_{k,i}(x_k, t) \rightarrow u_{k,i}(f(x_k, l), t) + c_i K(x_k). \quad (2)$$

Note that the advection function $e_{k,i}$ depends on both velocity components $u_{k,i}$ (with $i = \{1, 2, 3\} \wedge i \neq k$) due to c_i in Eq. (4). The mapping function $f(x_k, l)$, representing fluid transport, is measure preserving (the non-local analog of vanishing velocity divergence), continuous, and satisfies the requirement of scale locality (at most order-unity changes in property gradients). These indispensable physical requirements for $f(x_k, l)$ are satisfied by a triplet map, which places three compressed copies of the original profile $\{u_{k,i}(x_k), x_k \in [x_0, x_0 + l]\}$ in the eddy range. The middle copy is reversed to preserve continuity. The triplet map $f(x_k, l) \rightarrow x_k$ is:

$$f(x_k, l) = x_0 + \begin{cases} 3(x_k - x_0), & \text{if } x_0 \leq x_k \leq x_0 + \frac{1}{3}l \\ 2l - 3(x_k - x_0), & \text{if } x_0 + \frac{1}{3}l \leq x_k \leq x_0 + \frac{2}{3}l \\ 3(x_k - x_0) - 2l, & \text{if } x_0 + \frac{2}{3}l \leq x_k \leq x_0 + l \\ (x_k - x_0), & \text{else.} \end{cases} \quad (3)$$

In Eq. (2), $K(x_k)$ is a kernel function which in combination with the amplitudes c_i assures momentum and energy conservation and controls the energy redistribution among the velocity components. A possible definition is: $K(x_k) = x_k - f(x_k, l)$. This energy redistribution is a 1D interpretation of the pressure-fluctuation effect in a 3D flow and therefore is called pressure scrambling.

Determination of the amplitudes c_i requires additional modeling.

Kerstein et al. (2001) derive the amplitudes:

$$c_i = \frac{27}{4l} \left(-u_{K;k,i} + \text{sign}(u_{K;k,i}) \sqrt{u_{K;k,i}^2 + \sum_j \alpha T_{ij} u_{K;k,j}^2} \right); i \neq k, j \neq k \quad (4)$$

with the definition

$$u_{K;k,i} \equiv \frac{1}{l^2} \int u_{k,i}(f(x_k)) K(x_k) dx_k \quad (5)$$

and the transfer matrix

$$\alpha T = \alpha \begin{pmatrix} -1 & 1 \\ 1 & -1 \end{pmatrix}. \quad (6)$$

The free parameter α ensures the amplitudes c_i in Eq. (4) to be real values for $0 \leq \alpha \leq 1$. We choose $\alpha = 1/2$ corresponding to the equalization of the two component available energies in the present formulation.

During an eddy event, the transfer matrix T redistributes the turbulent kinetic energy among velocity components.

This ‘pressure scrambling’ accounts for the tendency for pressure fluctuations to restore isotropy and is invariant under exchange of indices. By construction the momentum and total energy are not changed by the pressure scrambling.

During the ODT time evolution in Eq. (1), the eddy size l and the location x_0 are sampled from a probability distribution representing the physics. For a given $\{l, x_0\}$ an eddy turnover time τ_e can be calculated leading to an occurrence frequency $\frac{1}{\tau_e}$. Since the ODT triplet map is an instantaneous process, the frequency for the eddy specified by $\{l, x_0\}$ is chosen from an event rate distribution:

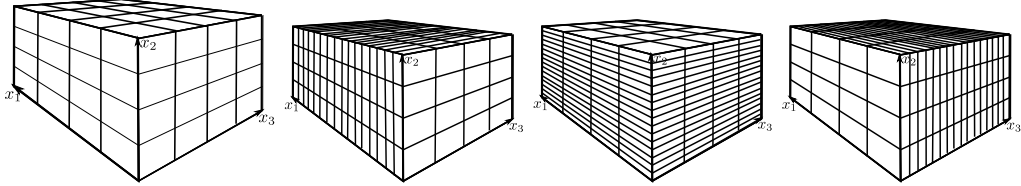
$$\lambda(x_0, l) = \frac{C}{l^2 \tau_e(x_0, l)} = \frac{C}{l^3} \sqrt{E_{kin} - E_{pot} - \frac{\nu^2}{l^2} Z} \quad (7)$$

involving particular definitions of the turbulent kinetic energy E_{kin} and the potential energy E_{pot} . The latter vanishes for the cases considered in this work. Note that the work by Ashurst and Kerstein (2005) introduces a variable density formulation of ODT including E_{pot} . The values l^{\max} , C , and Z are adjustable model parameters. The latter is introduced to cut off eddies with unphysically small energy and the parameter C is an overall rate coefficient determining the strength of the turbulence. The maximum eddy length l^{\max} is chosen to characterize the largest (global) scale within the flow, e.g. the channel half height.

3. Extended Large Eddy Simulation (XLES)

In sections 3.1, 3.2, and 3.4 the XLES framework is summarized briefly, to allow focus on features related to ODTLES without repeating details introduced in part I (Glawe et al. (2015)).

Additionally a time scale separation is introduced in section 3.3 to simplify the interpretation of microscale terms with reference to the ODT advancement.



(a) $[l_1 l_2 l_3] u_i = \bar{u}_i^{\text{LES}}$. (b) grid 1: for $\hat{u}_{1,i}$. (c) grid 2: for $\hat{u}_{2,i}$. (d) grid 3: for $\hat{u}_{3,i}$.

Figure 1: In XLES the velocity components u_i are resolved using multiple XLES-grids illustrated in 1b-1d. 3D large scale properties, corresponding to a standard LES grid with (illustrative) $N_{\text{LES}} = 4$ cells, are illustrated in 1a. Illustrative XLES-resolved small scale (‘RSS’) properties are approximated using $N_{\text{RSS}} = 16$ cells in 1b-1d.

3.1. XLES: Spatial Filtering

The basic XLES concept is to apply 2D filters to the velocity field, maintaining one Cartesian direction highly resolved. Using these filters, three 2D filtered velocity fields, each corresponding to one highly resolved Cartesian direction, are introduced and discretely represented by three staggered XLES-grids, illustrated in figure 1b – 1d.

A vector-matrix notation (which we will refer to as XLES-vector notation) is used to represent the three 2D filtered velocity fields:

$$\begin{pmatrix} [l_2 l_3] u_i \\ [l_1 l_3] u_i \\ [l_1 l_2] u_i \end{pmatrix} = \begin{pmatrix} l_2 l_3 & 0 & 0 \\ 0 & l_1 l_3 & 0 \\ 0 & 0 & l_1 l_2 \end{pmatrix} \begin{pmatrix} u_i \\ u_i \\ u_i \end{pmatrix} \equiv \underline{l}^{2D} \underline{u}_i \equiv \hat{u}_i, \text{ with } i = \{1, 2, 3\} \quad (8)$$

where i indexes the velocity components. We introduce another index k referring to the velocity field $\hat{u}_{k,i}$ represented in XLES-grid k (similar to the index notation in section 2).

Here without loss of generality (w.l.o.g.) the 2D filter operator $[l_2 l_3]$ (corresponding to XLES-grid 1) represents a tensor product of 1D filter operators $[l_2]$ and $[l_3]$. This tensor product is commutable: $[l_2 l_3] = [l_3 l_2]$.

The 1D filter operators are used to derive micro-and macroscale velocity terms:

$$\begin{aligned} u_i &= [l_1 l_2 l_3 + s_1 l_2 l_3 + l_1 s_2 l_3 + l_1 l_2 s_3] u_i \\ &\quad + \underbrace{[s_1 s_2 l_3 + s_1 l_2 s_3 + l_1 s_2 s_3 + s_1 s_2 s_3]}_{\equiv S \text{ (denoting XLES SGS terms)}} u_i. \end{aligned} \quad (9)$$

with the 1D small scale operator $s_k = \mathbb{1} - l_k$ ($k = \{1, 2, 3\}$) and the unity operator $\mathbb{1}$.

These scales are decomposed (using the 2D filter matrix $\underline{\underline{l}}^{2D}$):

$$\underline{u}_i = \begin{pmatrix} [l_2 l_3] u_i \\ [l_1 l_3] u_i \\ [l_1 l_2] u_i \end{pmatrix} + \begin{pmatrix} [l_1 s_2 l_3 + l_1 l_2 s_3] u_i \\ [s_1 l_2 l_3 + l_1 l_2 s_3] u_i \\ [s_1 l_2 l_3 + l_1 s_2 l_3] u_i \end{pmatrix} + \begin{pmatrix} [\mathcal{S}] u_i \\ [\mathcal{S}] u_i \\ [\mathcal{S}] u_i \end{pmatrix} \equiv \underline{\underline{l}}^{2D} \underline{u}_i + \underline{\underline{C}} \underline{\underline{s}}^{1D} \underline{\underline{l}}^{2D} \underline{u}_i + [\mathcal{S}] \underline{u}_i \quad (10)$$

into three terms:

1. ‘Directly Resolved’:
 $\underline{\underline{l}}^{2D} \underline{u}_i$ is discretely represented in the XLES-grids.
2. ‘Indirectly Resolved’:
 The resolved small scale (RSS) velocities

$$\tilde{u}_i \equiv \underline{\underline{s}}^{1D} \underline{\underline{l}}^{2D} \underline{u}_i = \hat{u}_i - \bar{u}_i^{\text{LES}} \quad (11)$$

(with $\bar{u}_i^{\text{LES}} = [l_1 l_2 l_3] u_i$) lead to coupling terms between the XLES-grids, and are directly resolved by another XLES-grid (see section 3.2 for details). The coupling matrix $\underline{\underline{C}}$ and the small scale matrix $\underline{\underline{s}}^{1D}$ are:

$$\underline{\underline{C}} = \begin{pmatrix} 0 & \mathbb{1} & \mathbb{1} \\ \mathbb{1} & 0 & \mathbb{1} \\ \mathbb{1} & \mathbb{1} & 0 \end{pmatrix} \text{ and } \underline{\underline{s}}^{1D} = \begin{pmatrix} s_1 & 0 & 0 \\ 0 & s_2 & 0 \\ 0 & 0 & s_3 \end{pmatrix}. \quad (12)$$

The LES velocity field \bar{u}_i^{LES} corresponds to the 1D filtered XLES velocity field: $[l_k] \hat{u}_{k,i}$ (see figure 1).

3. ‘Not Resolved’:

$$[\mathcal{S}] u_i = [s_1 s_2 l_3 + s_1 l_2 s_3 + l_1 s_2 s_3 + s_1 s_2 s_3] u_i \equiv \tilde{u}_i \quad (13)$$

is not resolved in any XLES-grid and leads to the XLES microscale terms.

Because the microscale model (ODT) is able to represent large scale effects and the macroscale model (XLES) contains 1D small scale terms, the classical term ‘scale separation’ is misleading for XLES and especially OD-TLES. Thus we will refer to a ‘filter separation’.

3.2. XLES: Momentum Conservation

The 2D filtered XLES momentum equations are

$$0 = \partial_{x_i} \bar{p}^{\text{LES}} + \left(\partial_t - \nu \sum_{j=1}^3 \partial_{x_j}^2 \right) \hat{u}_i + \sum_{j=1}^3 \partial_{x_j} \hat{u}_j * \hat{u}_i \quad (14)$$

$$+ \sum_{j=1}^3 \left(\underline{\mathcal{R}}_{ij}^{\text{XLES}} + \underline{\mathcal{C}}_{ij}^{\text{XLES}} + \underline{\mathcal{X}}_{ij}^{\text{XLES}} \right) + \underline{\sigma}^{\text{spatial}}$$

with the entry-wise multiplication $*$ between XLES-grid vectors (and matrices). The decomposed SGS Reynolds stresses $\underline{\mathcal{R}}_{ij}^{\text{XLES}}$ and the cross-stress terms $\underline{\mathcal{C}}_{ij}^{\text{XLES}}$ are combined to obtain the XLES sub-grid scale (SGS) advection terms:

$$\underline{l}^{2D} \underline{\mathcal{M}}_{ij} \equiv \underline{l}^{2D} \partial_{x_j} \left(\tilde{u}_j * \tilde{u}_i + \tilde{u}_j * \tilde{u}_i + \frac{1}{2} (\tilde{u}_j \bar{u}_i^{\text{LES}} + \bar{u}_j^{\text{LES}} \tilde{u}_i + \tilde{u}_i \tilde{u}_j) \right) \quad (15)$$

and its coupling $\underline{l}^\dagger * \underline{\mathcal{C}} \underline{l}^{2D} \underline{\mathcal{M}}_{ij}$. Here \tilde{u}_i is the vector notation for Eq. (13), \tilde{u}_i is defined in Eq. (11), and \underline{l}^\dagger is defined in Eq. (17).

The linearized coupling stress terms of the resolved small scale velocities \hat{u}_i are:

$$\underline{\mathcal{X}}_{ij}^{\text{XLES}} = \underline{l}^\dagger * \partial_{x_j} \underline{\mathcal{C}} (\hat{u}_j * \hat{u}_i - \bar{u}_j^{\text{LES}} * \bar{u}_i^{\text{LES}}), \quad (16)$$

which has a discrete representation. Hereby the matrix \underline{l}^\dagger with

$$\underline{l}^\dagger = \begin{pmatrix} \mathbb{1} & l_1^{-1} l_2 & l_1^{-1} l_3 \\ l_2^{-1} l_1 & \mathbb{1} & l_2^{-1} l_3 \\ l_3^{-1} l_1 & l_3^{-1} l_2 & \mathbb{1} \end{pmatrix} \quad (17)$$

includes the deconvolution operator l_k^{-1} which reconstructs filtered information. Due to the coupling the large scale influenced by highly resolved effects in a specific XLES-grid is communicated to the other XLES-grids. Hereby the reconstruction is executable because the operator $[l_k^{-1}]$ is only applied to large scale terms in x_k -direction. For details about the coupling procedure and an possible algorithm for a discrete deconvolution, please see (Glawe et al., 2015, section 3.1).

The spatial XLES model error terms are:

$$\underline{\sigma}^{\text{spatial}} = \partial_{x_j} \underline{l}^{2D} \mathbb{1} (\tilde{u}_{1,j} \tilde{u}_{2,i} + \tilde{u}_{1,j} \tilde{u}_{3,i} + \tilde{u}_{2,j} \tilde{u}_{1,i} + \tilde{u}_{2,j} \tilde{u}_{3,i} + \tilde{u}_{3,j} \tilde{u}_{1,i} + \tilde{u}_{3,j} \tilde{u}_{2,i}) + \underline{\mathcal{L}}_{ij}^{2D} \quad (18)$$

including non-linear coupling terms and the 2D Leonard stresses $\underline{\mathcal{L}}_{ij}^{2D}$.

3.3. XLES: Time Scale Separation

The XLES advection terms are represented by three overlapping XLES-grids, including coupling terms between these XLES-grids, and an additional ODT advancement for ODTLES. This ODT advancement involves instantaneous stochastic mappings whose instantaneous nature is in conflict with the idea of high order time integration schemes.

On the one hand, the simplest and physically most convenient way to advance the coupling terms and the dynamical SGM within an XLES framework is an explicit Euler scheme, which allows a straightforward interpretation of coupling terms and the stochastic turbulent advection within ODT.

On the other hand, an efficient numerical advection scheme includes high order time integration, which is even required for stability reasons by some spatial discretizations.

A known compromise is to linearize the advection: The linear advection part is advanced by a high order numerical scheme (details in part I (Glawe et al. (2015))), while the non-linear part is implemented by a 1st order explicit Euler scheme. One possible way to interpret such an approach is to integrate the dynamical velocity field over one time step and use this velocity field to advect the dynamical variables within the next time step. This approach can easily include random occurrences of instantaneous ODT mappings and therefore is suitable for ODTLES.

In part I ((Glawe et al., 2015, section 3.3)), alternative time schemes are suggested which potentially avoid the linearization of the advection terms.

In contrast to RaNS models, time averaging is not applied to the dynamical variables, but to the advecting velocity variables. This is especially reasonable because ODT is a dynamical model introducing small time scale effects.

Formally a time scale separation is invoked that simplifies the inclusion of ODT into XLES, though this procedure is not required by XLES (in part I (Glawe et al. (2015))) time scales are not separated). The separated time scales are:

$$u_j = \langle u_j \rangle + \{u_j\} \quad (19)$$

with the large time scale

$$\langle u_j \rangle = \frac{1}{\tau} \int_t^{t+\tau} u_j dt' \quad (20)$$

and the small time scale (fluctuations) $\{u_j\} = u_j - \langle u_j \rangle$. Note that the time filter and spatial filters in XLES are independent of each other: $\langle [l_k] u_j \rangle = [l_k] \langle u_j \rangle$.

The integral time τ corresponds to the 3D large scale flow. A natural choice for τ is the discrete time step size of the 3D large scale advancement scheme. Thus the modeling strategy is directly connected to the numerical realization.

If an explicit time integration scheme is used, τ is numerically restricted by a (global) Courant-Friedrichs-Lewy condition. Here CFL defines the constant CFL -number depending on the implemented numerical scheme:

$$\tau = CFL \min_{k,i} \left(\frac{\Delta x_k^{\text{LES}}}{\hat{u}_{k,i}} \right) \quad (21)$$

within all XLES-grids $k = \{1, 2, 3\}$ and with all velocity directions x_i ($i = \{1, 2, 3\}$). Local time step restrictions are possible but not implemented.

The time scale separation within XLES-U implies additional error terms caused by time scale separation:

$$\sigma_{XLES-U}^{\text{temporal}} = \sum_{j=1}^3 \partial_{x_j} \{ \hat{u}_{1,j} \} \hat{u}_{1,i}. \quad (22)$$

By defining the integral time scale τ based on the resolved small scale cell size Δx_k^{RSS} in XLES-grid k , the time scale separation is suppressed, because all XLES-U velocities are large scale in time:

$$\tau = CFL \min_{k,i} \left(\frac{\Delta x_k^{\text{RSS}}}{\hat{u}_{k,i}} \right) \quad (23)$$

The CFL -number can be used to switch between Eq. (21) and Eq. (23) and thus becomes a model parameter balancing (and controlling) the temporal model error $\sigma_{XLES-U}^{\text{temporal}}$ and the model performance.

Thus the CFL -number can be increased for performance reasons: OD-TLES is still stable and well defined for $CFL = 0.5 \frac{N_{\text{RSS}}}{N_{\text{LES}}}$ which e.g. for $N_{\text{RSS}} = 512$ and $N_{\text{LES}} = 16$ leads to a factor 32 increased XLES time-step size (ODT advancement is indirectly influenced) with additional model errors (see Eq. (22)) having only a small impact on specific problems. In this work all results are computed with considerably small CFL -number, following Eq. (23).

Since ODTLES allows a huge number of turbulent ODT events within the time scale τ , the averaged velocities are smoothed, which is part of the ODTLES modeling strategy. Again the CFL -number is controlling this modeling impact, because with τ based on Eq. (23) the number of ODT turbulent events is decreased.

ODT describes fluctuations (small time scale terms) in ODT-direction x_k corresponding to advection terms of the form $\partial_j \{\hat{u}_{k,k}\} \hat{u}_{k,i}$. The corresponding time averaged advecting velocity $\langle \hat{u}_{k,k} \rangle$ is specified due to mass conservation, see section 3.4. The terms $\partial_j \{\hat{u}_{k,k}\} \hat{u}_{k,i}$ correspond formally to the spatial XLES macroscale (they are part of the model error in Eq. (22), controlled by CFL), but can be interpreted by ODT, which is possible due to the time scale separation.

Additionally to the terms $\underline{\mathcal{M}}_{ij}$ ODT directly and indirectly (due to coupling) represents fluctuations across 3D large scale cells:

$$\sum_{j=1}^3 (\partial_{x_j} \{\hat{u}_j\} * \hat{u}_i + (\underline{\underline{C}} \partial_{x_j} \{\hat{u}_j\} * \hat{u}_i)^T) = (\underline{\underline{1}} + \underline{\underline{l}}^\dagger * \underline{\underline{C}}) \begin{pmatrix} \partial_{x_1} \{\hat{u}_{1,1}\} \hat{u}_{1,i} \\ \partial_{x_2} \{\hat{u}_{2,2}\} \hat{u}_{2,i} \\ \partial_{x_3} \{\hat{u}_{3,3}\} \hat{u}_{3,i} \end{pmatrix} + \underline{\underline{\sigma}}_{ODTLES}^{\text{temporal}}. \quad (24)$$

This model assumption leads to a model error term replacing Eq. (22):

$$\underline{\underline{\sigma}}_{ODTLES}^{\text{temporal}} = \begin{pmatrix} \partial_{x_2} \{\check{u}_{1,2}\} \check{u}_{1,i} + \partial_{x_3} \{\check{u}_{1,3}\} \check{u}_{1,i} \\ \partial_{x_1} \{\check{u}_{2,1}\} \check{u}_{2,i} + \partial_{x_3} \{\check{u}_{2,3}\} \check{u}_{2,i} \\ \partial_{x_1} \{\check{u}_{3,1}\} \check{u}_{3,i} + \partial_{x_2} \{\check{u}_{3,2}\} \check{u}_{3,i} \end{pmatrix}. \quad (25)$$

The error term in Eq. (25) summarizes all fluctuating terms not in ODT direction x_k . Again this error term is controlled by the CFL -number.

Applying the time scale separation to the advecting velocities leads to a modified XLES momentum equation (compare to Eq. (14)):

$$\begin{aligned} 0 = & \partial_{x_i} \langle \hat{p} \rangle + \left(\partial_t - \nu \sum_{j=1}^3 \partial_{x_j}^2 \right) \hat{u}_i + \sum_{j=1}^3 \partial_{x_j} \langle \hat{u}_j \rangle * \hat{u}_i \\ & + \underline{\underline{\mathcal{M}}}_{ODT} + \underline{\underline{\sigma}}^{\text{spatial}} + \underline{\underline{\sigma}}^{\text{temporal}} \\ & + \sum_{j=1}^3 \underline{\underline{l}}^\dagger * \partial_{x_j} \underline{\underline{C}} \left(\langle \hat{u}_j \rangle * \hat{u}_i - \langle \underline{u}_j \rangle^{\text{LES}} * \underline{u}_i^{\text{LES}} \right) + \underline{\underline{l}}^\dagger * \underline{\underline{C}} \underline{\underline{\mathcal{M}}}_{ODT}. \end{aligned} \quad (26)$$

The advection terms assumed to be modeled directly by ODT (involving 3 velocity components) are:

$$\underline{\mathcal{M}}_{ODT} = \sum_{j=1}^3 \left(\underline{l}^{2D} \underline{\mathcal{M}}_{ij}^{XLES} + \partial_{x_i} \{\underline{\hat{p}}\} + \partial_{x_j} \{\underline{\hat{u}}_j\} * \underline{\hat{u}}_i \right). \quad (27)$$

The derivation of $\underline{\mathcal{M}}_{ODT}$ is tailored for ODT, which is emphasized by the acronym ODT. Additionally the ODT advancement is coupled between the XLES-grids ($\underline{l}^\dagger * \underline{\mathcal{C}} \underline{\mathcal{M}}_{ODT}$).

Note that spatial large scale terms of the form $\partial_{x_2} \{\overline{u}_{1,2}^{LES}\} \overline{u}_{1,i}^{LES}$ are included in the ODT coupling $\underline{l}^\dagger * \underline{\mathcal{C}} \underline{\mathcal{M}}_{ODT}$.

The term $\partial_{x_i} \{\underline{\hat{p}}\} = \underline{l}^{2D} \partial_{x_i} \{\underline{p}\}$ describes pressure fluctuations. By construction ODT is mass conservative, nevertheless pressure fluctuations are modeled by applying the so called pressure scrambling (see section 2).

The full ODTLES advancement cycle is summarized in section 5.

An alternative approach, applied by Cline (2015) within the lattice-based multiscale simulation model (LBMS), is to couple each individual turbulent event within the ODT advancement, instead of the time averaging approach introduced here. This approach potentially introduces small time scale communication within a parallel algorithm.

3.4. XLES: Mass Conservation

In the incompressible flow regime, the 2D filtered velocity fields need to be divergence free to ensure mass conservation.

Because the XLES dynamics take place on the integral time scale (τ), the 2D filtered mass equation

$$0 = \sum_{i=1}^3 \partial_{x_i} \underline{l}^{2D} \langle \underline{u} \rangle_i = \sum_{i=1}^3 \partial_{x_i} \langle \overline{u}_i \rangle^{LES} + \sum_{i=1}^3 \partial_{x_i} \langle \check{u}_i \rangle \quad (28)$$

is enforced for the integral time scale by the procedure described in this section, while velocity fluctuations (corresponding to the small time scale), described by the ODT advancement, are mass conservative by construction (see section 2).

The mass conservation of the 3D large scale velocity $\langle \overline{u}_i \rangle^{LES}$ is enforced by a standard approach: A pressure Poisson equation is solved, leading to a large scale pressure field $\langle \overline{p} \rangle^{LES}$ (see standard textbooks, e.g. Ferziger

and Peric (1999)). The resulting pressure gradient $\partial_{x_i} \langle \underline{\bar{p}} \rangle^{\text{LES}}$ enforces a divergence free velocity field $\langle \underline{\bar{u}}_i \rangle^{\text{LES}}$ by solving: $\partial_t \langle \underline{\bar{u}}_i \rangle^{\text{LES}} + \partial_{x_i} \langle \underline{\bar{p}} \rangle^{\text{LES}} = 0$ (see section 5 and especially Eq. (36)). Here a consistent 3D large scale field $\langle \underline{\bar{u}}_i \rangle^{\text{LES}} = [l_1] \langle \hat{u}_{1,i} \rangle = [l_2] \langle \hat{u}_{2,i} \rangle = [l_3] \langle \hat{u}_{3,i} \rangle$ is required, which is enforced by the coupling terms $\langle \underline{\mathcal{X}}_{ij}^{\text{XLES}} \rangle$ and $\langle \underline{l}^\dagger * \underline{C} \underline{\mathcal{M}}_{\text{ODT}} \rangle$.

The resolved small scale (RSS) divergence $\sum_{i=1}^3 \partial_{x_i} \langle \underline{\hat{u}}_i \rangle = 0$ vanishes if a box filter $[l_k] \langle u_i \rangle = \frac{1}{\Delta x_k} \int_{-\frac{\Delta x_k}{2}}^{\frac{\Delta x_k}{2}} \langle u_i \rangle dx'_k$ is used (proof in ((Glawe et al., 2015, Appendix B))).

Since the 3D velocities $\langle \underline{\bar{u}}_j \rangle^{\text{LES}}$ are divergence free (after solving the pressure Poisson problem), a direct solver can compute one velocity component $\langle \hat{u}_{k,k} \rangle$ in each XLES-grid k within one 3D cell of the size Δx_k (w.l.o.g. in XLES-grid 1):

$$\begin{aligned} \langle \hat{u}_{1,1} \rangle \left(\frac{-\Delta x_1}{2} + x_1 \right) &= \langle \underline{\bar{u}}_1 \rangle^{\text{LES}} \left(-\frac{\Delta x_1}{2} \right) \\ &\quad - \int_{-\frac{\Delta x_1}{2}}^{-\frac{\Delta x_1}{2} + x_1} \partial_{x_2} \langle \hat{u}_{1,2} \rangle dx'_1 - \int_{-\frac{\Delta x_1}{2}}^{-\frac{\Delta x_1}{2} + x_1} \partial_{x_3} \langle \hat{u}_{1,3} \rangle dx'_1 \end{aligned} \quad (29)$$

for $x_1 \leq \Delta x_1$. Owing to the absence of a 3D small scale velocity field, small scale pressure effects vanish from the equations: $\langle \hat{p} \rangle = \langle \underline{\bar{p}} \rangle^{\text{LES}}$, but ODT explicitly models small time scale pressure effects (see section 2).

Because 9 velocity components within 3 XLES-grids are redundant, one dynamical velocity component in each XLES-grid is omitted by multiplying a matrix of Kronecker deltas

$$\underline{\mathbb{1}} - \underline{\delta}_i = \begin{pmatrix} 1 - \delta_{1i} & 0 & 0 \\ 0 & 1 - \delta_{2i} & 0 \\ 0 & 0 & 1 - \delta_{3i} \end{pmatrix} \text{ with } (1 - \delta_{ki}) = \begin{cases} 0, & \text{if } k = i \\ 1, & \text{else} \end{cases} \quad (30)$$

to the XLES momentum equation Eq. (26), leading to

$$\begin{aligned} 0 &= (\underline{\mathbb{1}} - \underline{\delta}_i) \partial_{x_i} \langle \underline{\bar{p}} \rangle^{\text{LES}} + \left(\partial_t - \nu \sum_{j=1}^3 \partial_{x_j}^2 \right) (\underline{\mathbb{1}} - \underline{\delta}_i) \underline{\hat{u}}_i \\ &\quad + (\underline{\mathbb{1}} - \underline{\delta}_i) \sum_{j=1}^3 \left(\partial_{x_j} \langle \underline{\hat{u}}_j \rangle * \underline{\hat{u}}_i + \underline{l}^\dagger * \partial_{x_j} \underline{C} \left(\langle \underline{\hat{u}}_j \rangle * \underline{\hat{u}}_i - \langle \underline{\bar{u}}_j \rangle^{\text{LES}} * \underline{\bar{u}}_i^{\text{LES}} \right) \right) \\ &\quad + \underline{\mathcal{M}}_{\text{ODT}}^\delta + \underline{l}^\dagger * \underline{C} \underline{\mathcal{M}}_{\text{ODT}}^\delta + (\underline{\mathbb{1}} - \underline{\delta}_i) \underline{\sigma}. \end{aligned} \quad (31)$$

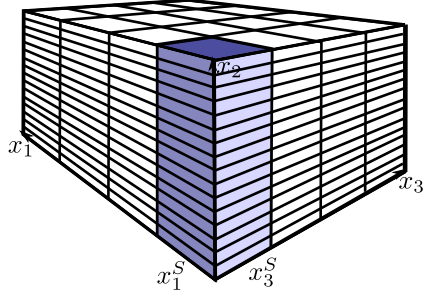


Figure 2: Illustrative 1D stack in XLES-grid 2 in x_2 -direction at (x_1^S, x_3^S)

Here terms to be modeled by the ODT model are

$$\underline{\mathcal{M}}_{ODT}^\delta = (\underline{\mathbb{1}} - \underline{\delta}_i) \sum_{j=1}^3 \left(\underline{l}^{2D} \underline{\mathcal{M}}_{ij}^{XLES} + \partial_{x_i} \{ \hat{p} \} + \partial_{x_j} \{ \hat{u}_j \} * \hat{u}_i \right) \quad (32)$$

and involve two velocity components orthogonal to the highly resolved direction in each XLES-grid (introduced in section 2).

4. From XLES to ODTLES

In this section ODT is interpreted as a microscale model within the XLES approach. In ODT a stochastic process mimics 3D turbulent advection within a 1D sub-domain. Thus, an interpretation of ODT in terms of the Navier-Stokes advection is not straightforward and ODTLES is not directly deducible from Navier-Stokes equations.

Nevertheless XLES microscale terms w.l.o.g. in XLES-grid 2 ($\mathcal{M}_{2,ODT}^\delta$ in Eq. (27)) are interpreted by $N_{LES_1} \times N_{LES_3}$ so called stacks, each containing highly resolved 1D information, e.g. defined by one line at (x_1^S, x_2, x_3^S) with constant x_1^S and x_3^S (see figure 2). The microscale terms $\mathcal{M}_{2,ODT}^\delta(x_1^S, x_2, x_3^S)$ in each of these stacks S contain 2 velocity components and can be modeled by the ODT advancement (Eq. (2)):

$$\mathcal{M}_{2,ODT}^\delta(x_1^S, x_2, x_3^S) = e_{2,i}(\hat{u}_{2,i}; x_2, l) + \sigma_{ODT_k}, \text{ and } l \leq l^{\max} = \Delta x_k^{LES} \quad (33)$$

with the ODT model error σ_{ODT_k} . Note that the ODT model introduced in section 2 also advances 2 velocity components which are orthogonal to the x_k -direction.

The maximum eddy length l^{\max} within the ODT model corresponds to the largest (global) scale. By using ODT as a model within the XLES framework, the maximum eddy size l^{\max} defines the boundary between turbulent scales described by the 3D advection scheme and by the ODT turbulent advection. Since ODT should capture turbulent effects not resolved by the 3D advection scheme, the maximum eddy size l^{\max} mainly depends on the numerical properties of the 3D advection scheme and needs to be determined by numerical tests (not shown here). We found $l^{\max} = \Delta x_k^{\text{LES}}$ to be convenient, which corresponds to the ability of the implemented numerical 3D advection scheme (see (Glawe et al., 2015, section 3.3)) to resolve e.g. the Kolmogorov length scale with approximately one 3D cell in the ‘DNS-limit’ of XLES (all scales are represented in 3D) as shown in part I ((Glawe et al., 2015, section 3.2)).

Closure of XLES can involve any form of modeling that specifies the RSS time advancement on an entire XLES-grid such as XLES-grid 2 shown in figure 2. This is not required to involve a collection of model instantiations on individual stacks, such as the illustrative stack in that figure. Nevertheless, sub-grid ODT within ODTLES is formulated in this way. On this basis, the XLES 3D advection can be viewed as a form of coupling of the ODT instantiations within one grid. In this context, the grid-to-grid coupling can be seen as a higher level of coupling. This is mentioned because previous ODTLES formulations did not envision the XLES framework with ODT not being the only conceivable RSS closure strategy within an XLES grid

In previous ODTLES formulations, pressure projection was the only grid-to-grid coupling. The insufficiency of this coupling is illustrated by a notional extension of the method to include passive scalar properties. These are not subject to pressure projection, so passive scalars on different grids would not be coupled at all, an obviously unsatisfactory situation. The present approach is straightforwardly extended to scalar properties in a manner that provides appropriate grid-to-grid coupling. This conceptual advantage of XLES does not imply that previous ODTLES formulations, which do not include scalars, are necessarily deficient in some way. Indeed, for reasons that are not entirely clear at present, they appear to perform well (Schmidt et al. (2008), Gonzalez-Juez et al. (2011)), with the caveat that the latter documented oscillations in velocity root mean squares that are not seen in results obtained using the present formulation (see sections 6.1 and 6.2).

4.1. ODTLES: ODT-limit

ODTLES includes another distinguished limit that we refer to as the ‘ODT-limit’: On the one hand ODTLES collapses to the ODT stand-alone model if only one 3D large scale cell represents the full domain. On the other hand the XLES microscale terms correspond to the full Navier-Stokes equations in this limit.

Thus the ODT model error σ_{ODT} can be estimated by comparing ODT and DNS results for a turbulent channel (see Appendix A).

The ability of ODT to describe the full spectrum of 3D turbulent effects is a required property to get an ODTLES 3D resolution largely independent of the turbulent intensity unless Reynolds-number variations trigger a global flow structure transition (see duct flow in section 6.3). Indeed, demonstrated model performance in the ‘ODT-limit’ (i.e. ODT stand-alone, see Appendix A) strongly indicates that ODT adequately describes the XLES model terms. This is also supported by ODTLES results that are shown to be in good agreement with DNS in sections 6.1, 6.2, and 6.3. Unfortunately a detailed theoretical investigation of the ‘ODT-limit’ requires a convenient ODT interpretation in Navier-Stokes terms, which is not derived to a satisfying level yet, but ensemble statistics are formally analogous to corresponding Navier-Stokes terms to a considerable extent (e.g. the interpretation of ODT budget terms of the turbulent kinetic energy in Appendix A).

4.2. ODTLES: ODT Modeling Effects

ODT introduces local turbulent events depending on the local flow state. In low Reynolds number channel flows the 3D grid is under-resolved only in the near-wall region (unless the grid is very coarse) and thus ODT works as a dynamical and highly accurate near-wall model, as figure 3a illustrates. For highly turbulent flows, the 3D resolution in the core region of the channel is under-resolved too: In this case ODT small scale eddy events additionally occur in the core region introducing local turbulent transport effects, as figure 3b illustrates.

In contrast to wall-modeled LES, the ODT turbulent transport treats all regions consistently without introducing additional assumptions for the near-wall region.

Additionally the ODT modeling depends on a fully resolved (1D) flow state and thus allows dominant small scale effects (e.g. local stratification, chemical processes, ...), which are not well captured by commonly applied eddy viscosity models.

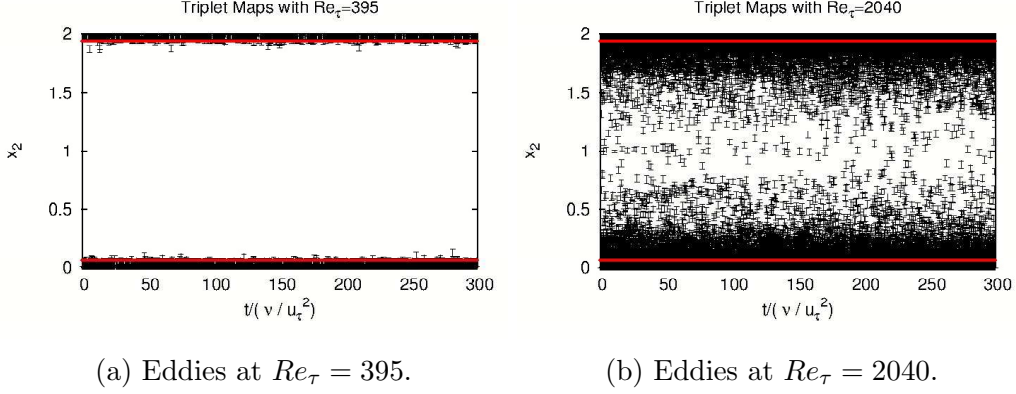


Figure 3: ODT turbulent events (‘eddies’) occurring in XLES-grid 2 (superposition of eddies in all ODT domains). The size of the 3D cell closest to the walls is illustrated by red lines ($N_{\text{LES}} = 32$). For low Reynolds numbers, ODT primarily acts as a near-wall model (3a); for high Reynolds numbers ODT acts as a sub-grid model over a larger extent of the flow domain (3b).

4.3. ODTLES: Coupled ODT Models

The turbulent ODT advection $e_{k,i}$ (in XLES-grid k) models the unresolved XLES terms $\mathcal{M}_{\text{ODT}_k}^\delta$. These are coupled across the XLES-grids due to the SGS coupling term $\underline{l}^\dagger * \underline{C} \mathcal{M}_{\text{ODT}}^\delta$ (see Eq. (31)). The ODT diffusion terms $\mathcal{D}_{\text{ODT}_k} = (-\nu) \partial_{x_k}^2 \hat{u}_{k,i}$ (for $k \neq i$) in XLES-grid k represent the molecular diffusion as a continuum and are connected to the XLES diffusion terms $(\underline{1} - \underline{\delta}_i)(-\nu) \sum_{j=1}^3 \partial_{x_j}^2 \hat{u}_{k,i}$: w.l.o.g. the XLES diffusion terms in grid 1

$$\nu \partial_{x_1}^2 \hat{u}_{1,i} + \nu \partial_{x_2}^2 \hat{u}_{1,i} + \nu \partial_{x_3}^2 \hat{u}_{1,i}, \quad \text{with } i = \{2, 3\} \quad (34)$$

are solved in three ways (compare to section 3.1):

1. Diffusion directly resolved by ODT: $\underline{\mathcal{D}}_{\text{ODT}}$
The terms $-\nu \partial_{x_1}^2 \hat{u}_{1,i}$ with $i = \{2, 3\}$ are interpreted by ODT incorporated in XLES-grid 1. These terms are resolved by N_{RSS} cells (representing molecular diffusion, similar to DNS)
2. Diffusion indirectly resolved by ODT: $\underline{l}^\dagger * \underline{C} \underline{\mathcal{D}}_{\text{ODT}}$
The terms $-\nu \partial_{x_2}^2 \hat{u}_{1,3}$ and $-\nu \partial_{x_3}^2 \hat{u}_{1,2}$ are interpreted by ODT domains residing in XLES-grid 2 respectively XLES-grid 3. W.l.o.g. the first term is coupled from XLES-grid 2 to XLES-grid 1 by $-[l_1^{-1}][l_2] \nu \partial_{x_2}^2 \hat{u}_{2,3}$ (index notation for $\underline{l}^\dagger * \underline{C} \underline{\mathcal{D}}_{\text{ODT}}$). The diffusion is fully resolved, but

additionally filtered (convolved) and deconvolved (see (Glawe et al., 2015, section 3.1)).

3. Diffusion resolved by XLES: $\underline{\mathcal{D}}_{\text{XLES}}$

The terms $-\nu\partial_{x_2}^2 \hat{u}_{1,2}$ and $-\nu\partial_{x_3}^2 \hat{u}_{1,3}$ are not interpreted by ODT in any XLES-grid (this is caused by $(\underline{\underline{1}} - \underline{\underline{\delta}}_i)$; see section 3.4). A numerical interpretation is possible within XLES-grid 1 using N_{LES} cells: $-\nu\partial_{x_i}^2 \hat{u}_{1,i}$ with $i = \{2, 3\}$. These diffusive terms are not resolved down to the molecular level. The XLES resolved diffusion terms are written as $\underline{\mathcal{D}}_{\text{XLES}}$ and numerically represented by an explicit Euler scheme in time and a spatial central difference scheme.

In summary the ODT model is incorporated into XLES-grid k by interpreting diffusive effects $\mathcal{D}_{\text{ODT}_k}$ and the microscale advection terms $\mathcal{M}_{\text{ODT}_k}^\delta$:

$$\mathcal{M}_{\text{ODT}_k}^\delta - \nu\partial_{x_k}^2 \hat{u}_{k,i} \approx e_{k,i} + \mathcal{D}_{\text{ODT}}(\hat{u}_{k,i}), \text{ for } i \neq k \quad (35)$$

Additionally the (diffusive and advective) ODT terms are coupled between the XLES-grids by $\underline{\underline{l}}^\dagger * \underline{\underline{C}}(e_i(\hat{u}_i) + \underline{\mathcal{D}}_{\text{ODT}}(\hat{u}_i))$. XLES diffusion terms $\underline{\mathcal{D}}_{\text{XLES}}$ are introduced to represent diffusive terms not captured by ODT.

The under-resolved diffusion terms $\underline{\mathcal{D}}_{\text{XLES}}$ are generally much smaller than the correct local diffusion and might be omitted in typical applications. Nevertheless these terms are conceptually desirable, because they allow the correct behavior in the ‘DNS-limit’.

5. ODTLES: Time Advancement

To advance the XLES equations in time a modified predictor-corrector procedure is used: The XLES momentum equations including coupling terms and ODT advancement are solved, predicting velocity fields in each XLES-grid. Simultaneously time averaged velocity fields are computed. A corrector step enforces the time averaged velocity fields to be divergence free (to ensure mass conservation).

Since the predictor-step involves ODT advancement and several coupling terms, a fractional time step algorithm is introduced:

1. predictor:

$$\hat{\underline{u}}_i^* = \hat{\underline{u}}_i(t) + \int_t^{t+\tau} \partial_{x_i} \langle \hat{\underline{p}} \rangle_t dt' \quad (36)$$

$$\hat{\underline{u}}_i^{**} = \hat{\underline{u}}_i^* + \int_t^{t+\tau} \sum_{j=1}^3 \partial_{x_j} \langle \hat{\underline{u}}_j \rangle_t * \hat{\underline{u}}_i^* dt' \quad (37)$$

$$\hat{\underline{u}}_i^{***} = \hat{\underline{u}}_i^{**} + \int_t^{t+\tau} \underline{l}^\dagger * \sum_{j=1}^3 \partial_{x_j} \left(\langle \hat{\underline{u}}_j \rangle_t * \hat{\underline{u}}_i^* - \langle \underline{\bar{u}}_j \rangle_t^{\text{LES}} * \underline{\bar{u}}_i^{*,\text{LES}} \right) dt' \quad (38)$$

$$\hat{\underline{u}}_i^{****} = \hat{\underline{u}}_i^{***} + \int_t^{t+\tau} (e_i(\hat{\underline{u}}_i^{****}) + \mathcal{D}_{\text{ODT}}(\hat{\underline{u}}_i^{****})) dt' + \int_t^{t+\tau} \mathcal{D}_{\text{XLES}}(\hat{\underline{u}}_i^{****}) dt' \quad (39)$$

$$\hat{\underline{u}}_i(t + \tau) = \hat{\underline{u}}_i^{****} + \int_t^{t+\tau} \underline{l}^\dagger * \underline{C} (e_i(\hat{\underline{u}}_i^{****}) + \mathcal{D}_{\text{ODT}}(\hat{\underline{u}}_i^{****})) dt' \quad (40)$$

2. corrector:

$$\text{1D filter} \quad \langle \underline{\bar{u}}_i \rangle_{t+\tau}^{\text{LES}} = \underline{l}^{1D} \langle \hat{\underline{u}}_i \rangle_{t+\tau} \quad (41)$$

$$\text{solve} \quad 0 = \sum_{i=1}^3 \partial_{x_i} \langle \hat{\underline{u}}_i \rangle_{t+\tau} \rightarrow \partial_{x_i} \langle \underline{\bar{p}} \rangle_{t+\tau}^{\text{LES}} \quad (42)$$

with $\langle \hat{\underline{p}} \rangle = \begin{pmatrix} l_1^{-1} & 0 & 0 \\ 0 & l_2^{-1} & 0 \\ 0 & 0 & l_3^{-1} \end{pmatrix} \langle \underline{\bar{p}} \rangle^{\text{LES}}$ (no small scale pressure field within XLES).

The subscript (e.g. $\langle \rangle_t$) introduced in time averaged properties indicates the time t (averaged over the last time step) respective $t + \tau$ (averaged over the actual time step with the time step size τ).

In the ODTLES advancement cycle the ODT advancement is the most costly sub-process which leads to a highly parallelizable algorithm.

The concrete numerical implementation of the individual steps Eq. (36–Eq. (40) is shown in Appendix B.

6. Application: Channel Case

6.1. ODTLES: Convergence Study

To verify the ODTLES model, we conduct a numerical convergence study by computing a turbulent channel flow with friction Reynolds number $Re_\tau = 395$.

In part I (Glawe et al., 2015, section 3.4) XLES-U (unclosed XLES) and LES-U (under-resolved, unclosed LES) results are compared to DNS by Kawamura et al. (1999) (online available: Kawamura (2014)): both LES-U and XLES-U converge towards DNS with increasing 3D resolution, but only XLES-U is able to represent the laminar sublayer independent of the 3D resolution. (The numerical schemes for LES-U and XLES-U are identical).

The ODTLES results are compared to XLES-U to show the significant effect of ODT as a SGM (see figure 4). Additionally the DNS results are presented for comparison reasons.

For this convergence study, both XLES and ODTLES are using $N_{LES} = \{16, 32, 64\}$ equidistant 3D large scale cells and $N_{RSS} = 512$ cells resolving the small scale.

The XLES time step size is limited by Eq. (23) with the Courant-Friedrichs-Lewy number $CFL = 0.45$ and the small scale cell size $\Delta x_{k,i}^{RSS}$ (the ODT advancement is only indirectly influenced by this CFL condition). This choice minimizes the temporal XLES error terms $\sigma_{XLES}^{temporal}$ introduced due to time scale separation (see section 3.3).

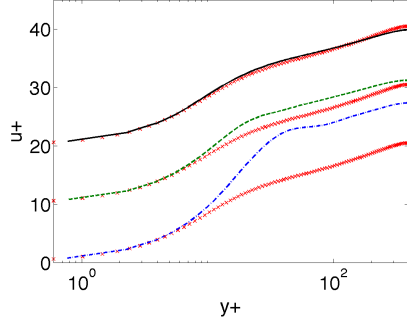
The ODT model parameters are $C = 6.5$ and $Z = 330$ and match the ODT stand alone simulation presented in Appendix A. The maximum eddy length l^{\max} in XLES-grid k equals the 3D large scale cell size Δx_k^{LES} .

To produce statistically significant results, the flow is averaged for $t_{ave} > 25$ non-dimensional time units (compared to $t_{ave} = 20$ for DNS) after reaching a steady state.

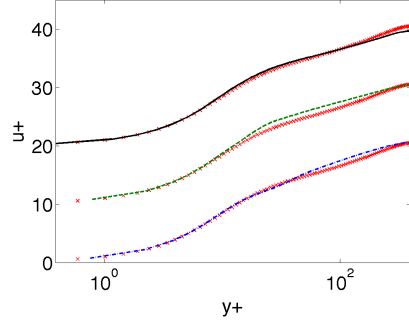
The mean velocity profiles computed by ODTLES (see figure 4b) and XLES (see figure 4a) are compared to DNS.

Additionally the streamwise and spanwise velocity RMS (see figure 4c) and the budget terms of the turbulent kinetic energy (see figure 4d–4f) are shown.

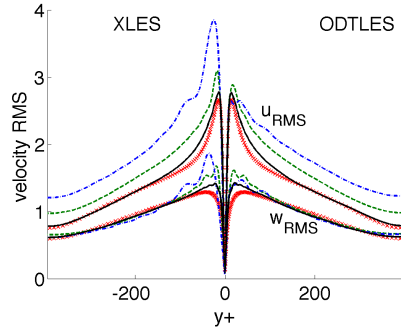
As derived in Kerstein et al. (2001) ODT pressure fluctuations cannot be distinguished from other turbulent transport terms. Thus we combine pressure terms into the turbulent transport also in ODTLES.



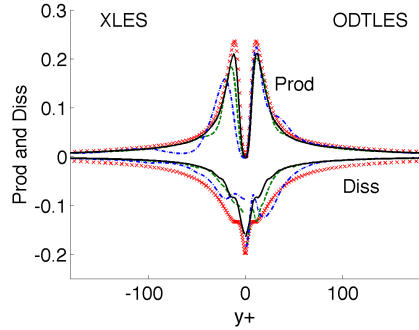
(a) XLES : law of the wall ($\hat{u}_{2,1}$). Profiles shifted with increasing N^{LES} .



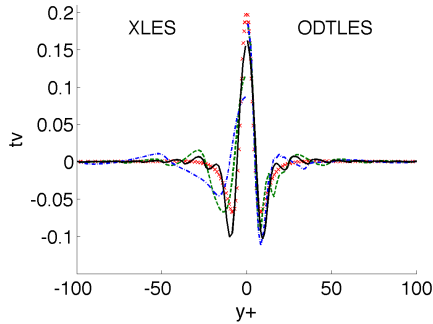
(b) ODTLES: law of the wall ($\hat{u}_{2,1}$). Profiles shifted with increasing N^{LES} .



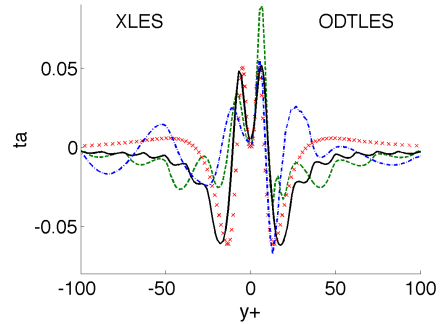
(c) Streamwise (u_{RMS}) and spanwise (w_{RMS}) velocity RMS.



(d) Production (Prod) and Dissipation (Diss) of the turbulent kinetic energy.



(e) Viscous transport of the turbulent kinetic energy (tv).



(f) Advective transport of the turbulent kinetic energy (ta).

Figure 4: Turbulent channel flow results for DNS (small red crosses), ODTLES, and XLES-U with $N_{\text{LES}} = 16$ (dash-dotted), $N_{\text{LES}} = 32$ (dashed), $N_{\text{LES}} = 64$ (solid). The small scales are resolved using $N_{\text{RSS}} = 512$ cells. The flow statistics are based on the velocity field $\hat{u}_{2,i}$.

XLES-U shows convergence towards the DNS results with increasing 3D resolution. ODTLES is able to represent the flow field and turbulent statistics even with the very low 3D resolution $N_{\text{LES}} = 16$, including the laminar sublayer near the walls and the budget terms of the turbulent kinetic energy. This significant improvement for channel flow results with very coarse 3D resolution compared to XLES-U suggests that ODTLES can encompass a wide Reynolds number range for fixed (coarse) 3D resolution. With increasing 3D resolution ODT-specific issues in the near-wall statistics decrease in ODTLES.

6.2. ODTLES: High Reynolds Number Flow

ODTLES combines the ability of the ODT model to describe all scales of highly turbulent flows within a 1D sub-domain of the full 3D domain with a coarse grained XLES approach representing the domain of e.g. a turbulent channel and introducing additional 3D effects compared to ODT stand-alone.

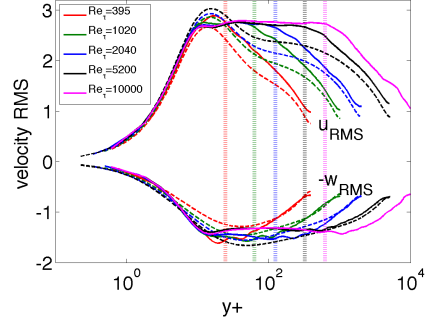
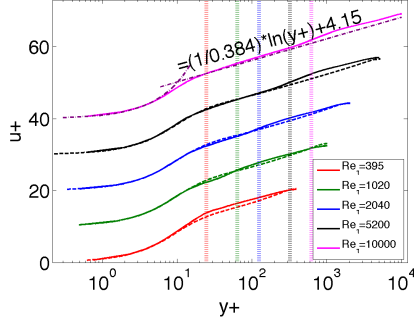
As shown in a convergence study in section 6.1 low Reynolds numbers are well described by ODTLES with only $N_{\text{LES}} = 16$ 3D cells. To demonstrate the ODTLES ability to describe highly turbulent flows within a simple domain, we conduct turbulent channel flow computations with $N_{\text{LES}} = 32$ cells (in 3D) and up to $N_{\text{RSS}} = 16384$ cells to represent additional small scale effects, which allows Reynolds numbers $Re_\tau \leq 10000$.

The CFL number is chosen following Eq. (23) with $CFL \leq 1$ and ODT parameters are: $C = 6.5$, $Z = 330$, and $l^{\max} = \Delta x_k^{\text{LES}}$.

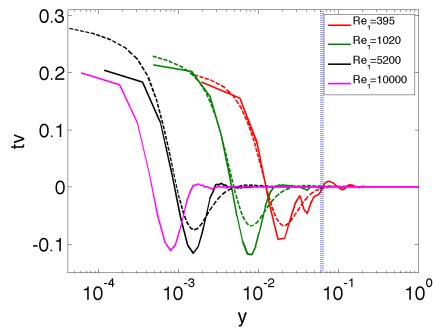
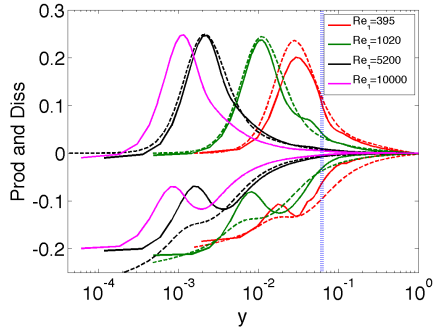
The mean velocity profiles for several friction Reynolds numbers are illustrated in figure 5a and compared to DNS by Kawamura et al. (1999) and Lee and Moser (2014a) (online available: Kawamura (2014) and Lee and Moser (2014b)). The ODTLES computation with $Re_\tau = 10000$ is in good agreement with the laminar solution near the wall and the law of the wall with a von Kármán constant $\kappa = 0.384$, as obtained by Lee and Moser (2014a) for $Re_\tau = 5200$.

The streamwise and spanwise velocity RMS (see figure 5b) are in good agreement with the available DNS in the laminar region near the wall and beyond the first 3D cell. The size of the first 3D cell is illustrated by vertical lines for the different Re_τ values. Within the first 3D cell, ODT typically has some issues in representing the velocity RMS (this also applies for the budget terms of the kinetic energy).

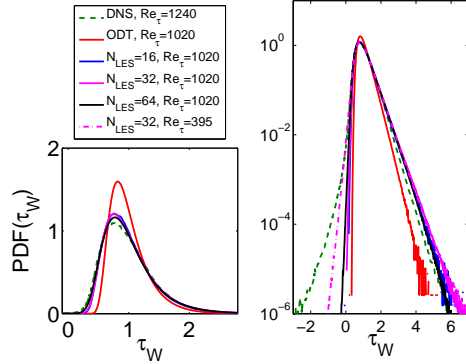
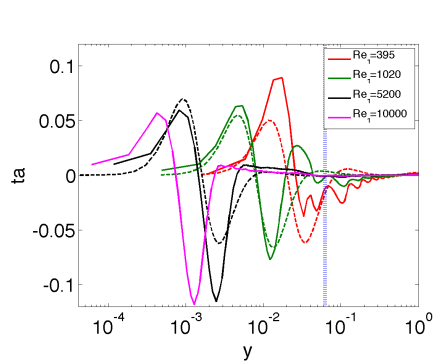
In figure 5c–5e the budget terms of the turbulent kinetic energy are shown to be in good agreement with the DNS results, especially for highly turbulent



(a) Law of the wall. Profiles shifted with increasing Re_τ . (b) Streamwise (u_{RMS}) and spanwise ($-w_{RMS}$) velocity RMS.



(c) Production (Prod) and Dissipation (Diss) of the turbulent kinetic energy. (d) Viscous transport of the turbulent kinetic energy (tv).



(e) Advective transport of the turbulent kinetic energy (ta). (f) Wall shear stress τ_W : linear (left) and logarithmic (right).

Figure 5: Turbulent channel flow results for ODTLES (solid) and available DNS (dashed) for $N_{LES} = 32$ (if not indicated otherwise) and with $N_{RSS} = 512$ (for $Re_\tau = 395$), $N_{RSS} = 2048$ (for $Re_\tau = 1020$), $N_{RSS} = 4096$ (for $Re_\tau = 2040$), $N_{RSS} = 8192$ (for $Re_\tau = 5200$), and $N_{RSS} = 16483$ (for $Re_\tau = 10000$). Figure 5f compares the ODT and ODTLES wall shear stress ($Re_\tau = \{395, 1020\}$) for various N_{LES} to DNS ($Re_\tau = 1240$).

flows.

ODT and ODTLES wall shear stress statistics for $Re_\tau = 1020$, illustrated in figure 5f, are compared to DNS results by Schlatter and Örlü (2010) for $Re_\tau = 1240$. The ODT wall shear statistics are in rather good agreement with the DNS (see figure 5f left), which indicates ODT to be an accurate near-wall model, yet by including additional 3D resolution N_{LES} within ODTLES the PDF is significantly improved. A more detailed investigation (see figure 5f right) shows that ODTLES underestimates rare backflow events. The reason could be that the responsible 3D structures near the wall are not represented due to the coarse 3D resolution, because the 3D cell size in wall units is $\Delta x^{\text{LES},+} \approx 32$ for the highest considered 3D resolution $N_{\text{LES}} = 64$ (with $Re_\tau = 1020$). The result with lower Reynolds number ($Re_\tau = 395$) with 3D cell size in wall units $\Delta x^{\text{LES},+} \approx 24.7$ supports this hypothesis. Here we assume a low Reynolds number sensitivity of the wall shear stress statistics, as Schlatter and Örlü (2010) report.

In summary ODTLES is able to capture the mean flow and turbulence statistics of highly turbulent flows up to $Re_\tau = 10000$ within a simple domain. The computational costs are significant lower compared to DNS: Lee et al. (2013) report to use about 260×10^6 CPU hours on 786×10^3 cores for the DNS with $Re_\tau = 5200$, while the corresponding ODTLES simulation takes ≈ 10000 CPU hours on 24 cores.

A detailed investigation of the expected computational costs relative to RaNS, LES and DNS in section 7 shows ODTLES to be convenient to describe highly turbulent flows in domains of moderate complexity.

6.3. ODTLES: Square Duct Flow

Sections 6.1 and 6.2 show turbulent channel flow results for the ODTLES model to be in good agreement with DNS. With increasing 3D resolution a convergence to DNS is observed, but even within an ‘ODT-limit’ (corresponding to a single 3D cell) the ODT model reproduces key flow features stand-alone (see Appendix A).

In this section the square duct flow is investigated. This flow combines a simple geometry (see figure 6a) and a complex flow behavior including secondary instabilities (secondary flow of Prandtl’s second kind) and turbulent fluctuations. These secondary instabilities represent a 3D flow phenomena which is not captured by the ODT model. For low Reynolds numbers (near the value for sustained turbulence) the size of the secondary flow structures in cross-stream direction corresponds to the half duct height (h). This flow

regime in a square duct is investigated by Uhlmann et al. (2007) using DNS. Even for higher Reynolds number the cross-stream extension of the secondary instabilities is rather large scale compared to turbulent fluctuations occurring e.g. near the wall. Nevertheless these small scale fluctuations play an important role for the duct flow because they generate secondary instabilities. The ODT model was shown to accurately describe small scale fluctuations and the secondary instabilities correspond to a rather large scale 3D flow feature which can be described by the XLES framework. Thus ODTLES is a highly promising model to describe the duct flow behavior, as Gonzalez-Juez et al. (2011) and Glawe et al. (2013) showed in previous ODTLES studies. In these works no coupling terms (last line in Eq. (26)) between the XLES-grids are considered.

The CFL number is chosen following Eq. (23) with $CFL \leq 1$. The ODT model parameters are $C = 6.5$, $Z = 330$, and $l^{\max} = \Delta x_k^{\text{LES}}$, which is identical to the channel flow setup in section 6.2.

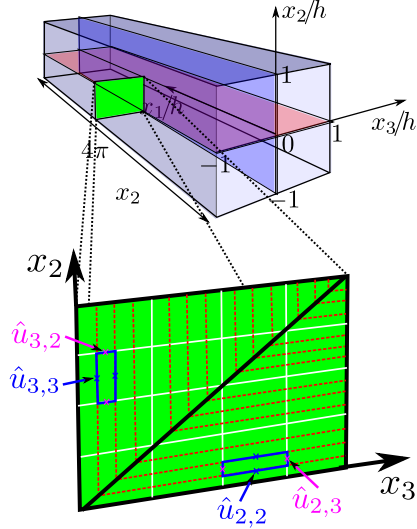
The flow is averaged for $t_{\text{ave}} u_B / h \geq 2800$ non-dimensional time units (with the bulk velocity u_B) after reaching a steady state which is assumed to be sufficient to investigate the secondary instabilities. This is supported by a study of vortex structures by Uhlmann et al. (2007) where nearly symmetric 8-vortex structures are observed for lower averaging times at the investigated Reynolds numbers $Re_B \geq 2600$. Additionally the ODTLES results are averaged over the 4 quadrants. Note that the DNS by Pinelli et al. (2010) uses $t_{\text{ave}} u_B / h \geq 7000$ to produce meaningful high order statistics.

Figure 6 compares the secondary flow computed by ODTLES for a moderate bulk Reynolds number $Re_B \approx 2600$ with the DNS by Pinelli et al. (2010) (online available: Uhlmann (2013)). Hereby ODTLES uses $N_{\text{LES}} = \{16, 32\}$ 3D large scale cells per direction and the XLES specific small scale properties are resolved by $N_{\text{RSS}} = 512$ cells.

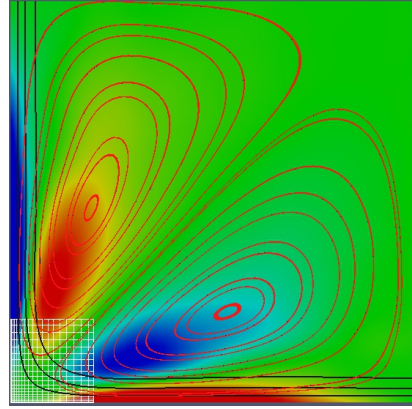
The primary flow and key features of the secondary flow are in good agreement with the DNS results even with the very low 3D resolution of $N_{\text{LES}} = 16$ cells. Furthermore the ODTLES results indicate a convergence towards the DNS results with increasing 3D resolution.

The secondary mean velocity field alters with increasing Reynolds number, as investigated in figure 7. In particular each secondary vortex structure tends towards a triangular shape for increasing Reynolds number. The vorticity approaches the duct corner with increasing Reynolds number, indicating fast changes in secondary flow directions in this area.

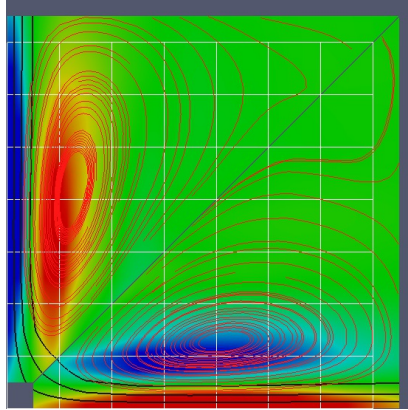
ODTLES results show a tertiary instability above some threshold Reynolds



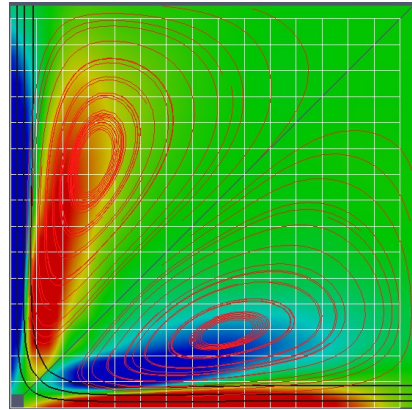
(a) Geometry and illustrated XLES-grids.



(b) DNS: $Re_B = 2600$.

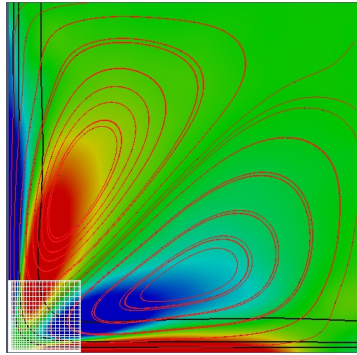


(c) ODTLES: $N_{LES} = 16$, $Re_B = 2667$.

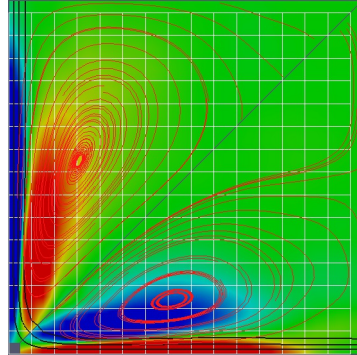


(d) ODTLES: $N_{LES} = 32$, $Re_B = 2514$.

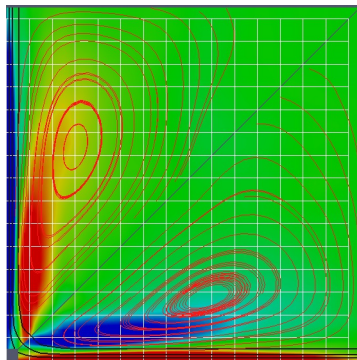
Figure 6: All results are averaged in time and streamwise direction. One quadrant of the duct is shown (see 6a). The 3D grid is indicated by white lines (for the DNS only in the corner region). ODTLES properties are illustrated like cell centered and show additional small scale features (resolved by $N_{RSS} = 512$ cells) using the XLES-grid highly resolved in vertically x_2 -direction (horizontally x_3 -direction) in the lower right (upper left) triangular region, as illustrated in 6a. Contour lines of the primary mean flow (black) for $u_1 = \{0.2, 0.4, 0.6\} \max(u_1)$, streamlines of the secondary mean flow (u_2, u_3) in red and the 2D vorticity $\omega_{2D} = \partial_{x_2} u_3 - \partial_{x_3} u_2$ (RGB color coded) are shown.



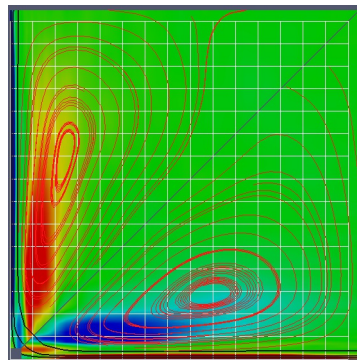
(a) DNS:
 $Re_B = 3500$.



(b) ODTLES:
 $Re_B = 3485, N_{RSS} = 1024$.

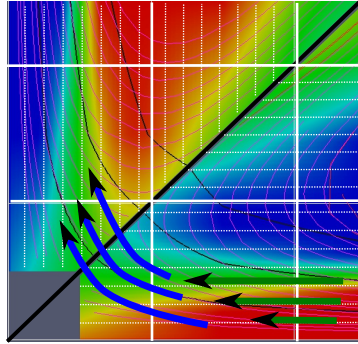


(c) ODTLES:
 $Re_B = 8446, N_{RSS} = 2048$.

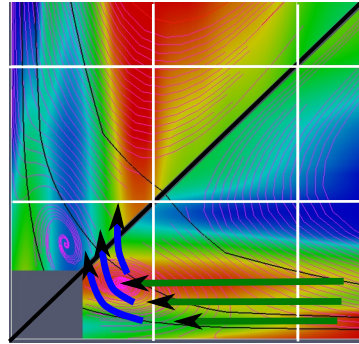


(d) ODTLES:
 $Re_B = 17338, N_{RSS} = 2048$.

Figure 7: ODTLES and DNS square duct results with $N_{LES} = 32$ for different Reynolds numbers Re_B . Primary and secondary streamlines and vorticity are illustrated similar to figure 6.



(a) $Re_B = 3485$, $N_{RSS} = 1024$.



(b) $Re_B = 17338$, $N_{RSS} = 2048$.

Figure 8: Zoom into the corner region of figure 7b ($Re_B = 3485$) and 7d ($Re_B = 17338$). Primary and secondary streamlines and vorticity are illustrated similar to figure 6. ODTLES properties are illustrated like cell centered (this leads to the gap in the flow field at the corner). 8a additionally shows the small scale resolution (illustrative with $N_{RSS} = 256$). An exemplary cross-stream flow approaches the corner parallel to the horizontal wall (green arrows) with wall-normal velocity gradients highly resolved only in the XLES-grid 2 (compare to figure 6a). Near the corner the vertical wall forces a flow stagnation and an associated pressure gradient drives the flow in the horizontal direction (blue arrows) which is highly resolved only in XLES-grid 3. For high Reynolds number duct flows (8b) both effects occur within one 3D cell, which is not well represented by ODTLES because the coupling procedure only communicates small scale effects affecting the large scale. This could lead to unphysical flow behavior within the 3D cell containing the corner.

number (between 8446 and 17338) in the corner region. This model result is not conclusive because the tertiary instability is not resolved sufficiently in 3D (see figure 8).

The 3D tertiary structure in the corner region is of similar size as the corresponding 3D computational cell. Its influence on the flow is primarily local. The insufficient 3D resolution possibly leads to an under-resolved pressure gradient which could prevent an adequate change of a fluid parcel’s direction (blue arrows within figure 8). Nevertheless the cross-stream flow is adequately resolved in the wall-normal direction (green arrows within figure 8). More reliable and conclusive results might be possible through future DNS studies.

ODTLES demonstrated its ability to describe and predict non-trivial flow behavior including secondary instabilities within a duct flow. We suspect that the flow transition leading to tertiary instability is a model artifact, although a physical cause cannot be ruled out until definitive evidence such as a DNS result becomes available. Nevertheless the tertiary structure is very local and not preventing the ODTLES model from describing the key flow features of the primary and secondary flow.

7. ODTLES: Resolution Properties and Efficiency

Different turbulence models, e.g. RaNS, wall-modeled LES (LES including a near-wall model), wall-resolved LES (LES with near wall resolution) and ODTLES, differ strongly in both represented physical effects and computational effort. In this section the computational costs of the different model approaches are estimated by developing a relation between the grid-size (used as a measure for the computational effort) and the Reynolds number following Chapman (1979) and especially Choi and Moin (2012) and references cited therein.

The investigated domain is a box of size $L_1 \times L_2 \times L_3$. A highly turbulent boundary layer over a flat-plate airfoil of the thickness δ fills the volume $[x_0, L_1] \times \delta(x_1) \times L_3$. The flow is assumed to reach the plate at $x_1 = x_0$ with a turbulent intensity Re_{x_0} . The boundary layer size $\delta(x_1)$ increases until reaching $x_1 = L_1$ with a corresponding Reynolds number Re_{L_1} . The number of grid cells N within the turbulent boundary layer is estimated for ODTLES and compared to RaNS, LES and DNS.

From Choi and Moin (2012) we extract the Reynolds dependent grid size

for RaNS and wall-modeled LES:

$$N_{RaNS|wm} = 54.7 \frac{L_3}{L_1} n_1 n_2 n_3 Re_{L_1}^{2/7} \left[\left(\frac{Re_{L_1}}{Re_{x_0}} \right)^{5/7} - 1 \right], \quad (43)$$

for a wall-resolved LES

$$N_{wr} = 0.021 \frac{L_3}{L_1} \frac{n_{2,laminar}}{\Delta x_{1,w}^+ \Delta x_{3,w}^+} Re_{L_1}^{13/7} \left[1 - \left(\frac{Re_{x_0}}{Re_{L_1}} \right)^{6/7} \right], \quad (44)$$

and for DNS

$$N_{DNS} = 0.000153 \frac{L_3}{L_1} Re_{L_1}^{37/14} \left[1 - \left(\frac{Re_{x_0}}{Re_{L_1}} \right)^{23/14} \right]. \quad (45)$$

Here $n_x n_y n_z$ is the number of grid points within the cube $\delta \times \delta \times \delta$, $n_{2,laminar}$ is the number of wall-normal grid points within the laminar sublayer, and $x_{k,w}^+$ is the LES cell size in wall units.

Following Chapman (1979) RaNS typically resolves the cube $\delta \times \delta \times \delta$ using $n_x n_y n_z \approx 1 \times 20 \times 0.5 = 10$ cells, while for wall-modeled LES Choi and Moin (2012) report typical grid resolutions $n_x n_y n_z \approx [1200, 33000]$. In wall-resolved LES Choi and Moin (2012) find typical resolution values $\frac{n_{2,laminar}}{\Delta x_{1,w}^+ \Delta x_{3,w}^+} \approx [\frac{1}{390}, \frac{1}{25}]$.

Here LES models represent turbulent scales down to the inertial range of the turbulent cascade. The ODT model, applied within XLES, potentially describes the full turbulent cascade within a 1D sub-domain, which leaves the 3D grid to capture non-turbulent effects (e.g. the domain or secondary instabilities). For the flat-plate airfoil even ODT stand-alone potentially leads to reasonable results for the case of a turbulent boundary layer (Lignell et al. (2013) apply ODT to a comparable turbulent case, but including buoyancy, by spatially advancing the ODT line). In consequence the (equidistant) XLES 3D resolution N_k in x_k -direction is chosen independently of the Reynolds number (unless Reynolds-number variations triggers a global flow structure transition, like the secondary instabilities in a turbulent duct).

In the current ODTLES implementation the resolved small scales are represented by N_{RSS_k} equidistant cells in x_k -direction ($k = \{1, 2, 3\}$). Following Choi and Moin (2012) for highly turbulent flows the number of grid points resolving the Kolmogorov length scale along a small distance dx_1 is

$N_1 = 0.116 \frac{dx_1}{x_1} Re_x^{13/14}$. Equidistant ODTLES uses the smallest length scale globally in all 1D sub-domains, leading to

$$N_{ODTLES} = 0.116 K_{ODT} N_1 N_3 \frac{L_3}{L_1} Re_{L_1}^{13/14} \quad (46)$$

A factor $K_{ODT} \approx 3 \times 6$ takes into account that 3 XLES-grids are used (we assume that $N_1 = N_2 = N_3$) and equidistant ODT uses at least 6 cells to allow a turbulent event (eddy) within the Kolmogorov scale.

In principle ODTLES can be extended to non-equidistant grids within the 1D sub-domain, which is for example realized by the adaptive ODT (aODT) implementation by Lignell et al. (2013). Although adaptive ODT is not used as a sub-grid model within an XLES approach yet, we investigate this interesting case as a worthwhile perspective and refer to it as aODTLES. For an adaptive grid we assume on average a resolution similar to DNS (in 1D) and integrate over the boundary layer thickness with $\frac{\delta}{x} = 0.16 Re_x^{-1/7}$ (see Choi and Moin (2012)) in the 1D sub-domain, leading to

$$N_{aODTLES} = 0.0103936 K_{aODT} N_1 N_3 \frac{L_3}{L_1} Re_{L_1}^{11/14} \left[1 - \left(\frac{Re_{x_0}}{Re_{L_1}} \right)^{25/14} \right]. \quad (47)$$

For adaptive ODT, note that we assume $K_{aODT} = 3$ because 3 XLES-grids are required (here we assume each XLES-grid uses the same RSS resolution and $N_1 = N_2 = N_3$). There is no additional assumption of a minimum number of cells representing the Kolmogorov length.

We compare typical RaNS and LES resolutions (following Choi and Moin (2012) and Chapman (1979)) with the ODTLES and aODTLES approach for different 3D resolutions in figure 9. Additionally numerical computations for a turbulent channel are shown assuming a similarity of the turbulent Reynolds number in the channel and Re_{L_1} . Hereby the DNS by Lee and Moser (2014b) (we assume $N \approx 8.5 \times 10^9$, estimated for $L_3/L_1 = 4$), an aODT result by Meiselbach (2015b) ($N_{aODT} \approx [80000, 120000]$ (Meiselbach (2015a))) and the ODTLES result with $Re_\tau = 10000$ in section 6.2 are used.

For weakly turbulent flows, ODTLES is subject to additional computational costs compared to standard LES. But ODTLES requires 3D resolution independent of the turbulence intensity (except secondary effects), and thus highly turbulent flows in moderately complex domains are well described with low computational costs. In some flow regimes ODTLES is more efficient than wall-modeled LES and although it represents advective and diffusive effects down to the Kolmogorov length scale. Incorporating adaptive

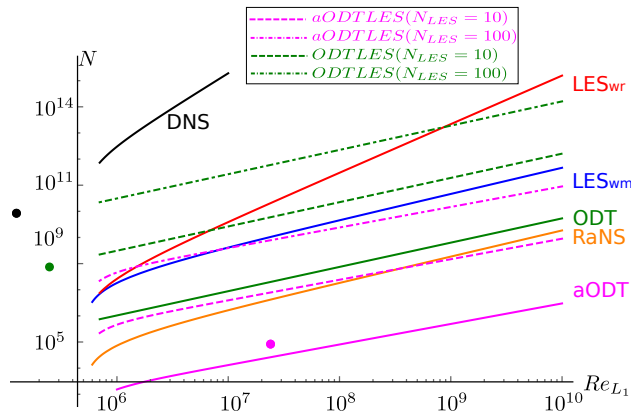


Figure 9: Number of grid points N required for numerical simulations of a flow over a flat-plate airfoil with aspect ratio $L_3/L_1 = 4$ and a turbulent inflow with $Re_{x_0} = 5 \times 10^5$. Wall-modeled LES ($n_1 n_2 n_3 = 2500$), wall-resolved LES ($n_{2,laminar}/\Delta x_{1,w}^+ \Delta x_{2,w}^+ = 1/200$), RaNS ($n_1 n_2 n_3 = 10$), ODTLES and aODTLES (ODTLES with adaptive ODT) with $N_1 = N_3 = \{10, 100\}$ cells, and the ODT and adaptive ODT (aODT) stand-alone model. Additionally, actual simulation cases for a turbulent channel (assuming $Re_{turb} \approx Re_{L_1}$) are shown for DNS ($Re_\tau = 5200$, black point), ODTLES ($Re_\tau = 10000$, green point), and aODT ($Re_\tau = 6 \times 10^5$, magenta point).

ODT into a XLES framework seems to be an especially promising alternative to wall-modeled LES and even RaNS simulations for highly turbulent flows in simple domains (requiring low 3D resolutions).

Note that in the presented estimation the costs of the computation within one discrete cell is neglected, because the different modeling strategies typically vary by a low factor ($\lesssim 2$), which is not strongly affecting the estimation in figure 9.

8. Conclusions

Part I (Glawe et al. (2015)) introduces XLES, an extended LES approach, which is a new strategy to simulate complex turbulent flows. The ODTLES model is one special approach in the XLES family of models, employing ODT as a sub-grid model. XLES in general and especially ODTLES are designed to describe highly turbulent flows in domains of moderate complexity. These problems especially occur in fundamental research studies of e.g. atmospheric flows and are also relevant in engineering.

A previous ODTLES version (by Schmidt et al. (2008) and Gonzalez-Juez et al. (2011)) can also be interpreted as ODT closed XLES, but with XLES velocities only coupled by a pressure projection. Thus oscillations in root mean square velocities occur (reported by Gonzalez-Juez et al. (2011)), but without significantly affecting mean profiles. The introduced XLES coupling terms directly carry over to scalar properties residing on different XLES-grids (e.g. required for a heated duct flow) which is a unsolved problem within the previous ODTLES formulation.

XLES time advances multiple coupled 2D filtered Navier-Stokes realizations, each having one Cartesian direction that is highly resolved. A one-dimensional modeling approach like ODT takes advantage of the specific symmetry of a 2D filter.

Especially within ODTLES, the ability of ODT to describe the full turbulent spectrum allows strongly reduced 3D resolutions without corrupting key flow features.

In XLES, separated physical effects (contrary to separated 3D scales in LES) are represented by appropriate approaches: the 3D resolution represents the 3D domain and other physical effects not captured by ODT, e.g. secondary instabilities (see section 6.3), while turbulent effects, not captured by XLES, are appropriately represented by the ODT sub-grid model. This

includes the representation of molecular diffusion and turbulent advection at the Kolmogorov length scale (within a 1D sub-domain).

ODTLES accurately describes a turbulent channel flow up to friction Reynolds number $Re \leq 10000$ with high accuracy, even with coarse 3D resolution (e.g. $N_{LES} = 16$ cells per direction) and is able to reproduce the primary and secondary flow in a square duct with similar 3D resolution.

The focus of this work is to introduce the mathematical framework necessary to derive the XLES approach, which is one possible way to incorporate ODT into 3D simulations. This is implemented here for a simple ODT model to avoid e.g. interpolation effects that are introduced by the adaptive ODT model by Lignell et al. (2013). Adaptive ODT outperforms the turbulence intensity reachable by equidistant ODT, as Meiselbach (2015b) recently showed using adaptive ODT simulations up to $Re_\tau \leq 6 \times 10^5$.

Incorporating this adaptive ODT model into the XLES filter approach can potentially serve as an alternative to RaNS simulations in industrial applications and additionally include a wide range of small scale physical effects, e.g. for flows including Prandtl number effects and combustion.

Various additional physical effects, e.g. additional scalar fields, are well tested for ODT and can easily be adapted to ODTLES. Furthermore the XLES framework is the first approach which consistently couples scalar properties and velocities between XLES-grids (in the previous ODTLES version only velocities were coupled). This enables ODTLES to compute e.g. fundamental meteorological flows.

Thus ODTLES accurately describes highly turbulent flows including fully resolved small scale effects with low computational costs for simple domains.

Acknowledgments

The authors would like to thank H. Kawamura and colleagues and R. Moser and colleagues for providing DNS results online (Kawamura (2014) and Lee and Moser (2014b)) as well as Philipp Schlatter and colleagues (Schlatter and Örlü (2010)) for providing τ_W statistics for comparison. This work was supported by the Brandenburg University of Technology Cottbus-Senftenberg, the Helmholtz graduate research school GeoSim, and the Freie Universität Berlin.

Appendix A. ODT: Illustrative Results

As discussed in section 4, ODT error terms σ_{ODT} can roughly be estimated by comparing ODT and DNS flow statistics. The turbulent channel is an appropriate study case for ODT because of its distinct predominant direction. ODT results with friction Reynolds number $Re_\tau = 395$ are compared to DNS (Kawamura (2014)), which allows additional comparison to LES-U and XLES-U results in (Glawe et al., 2015, section 3.4) and ODTLES results in section 6.1.

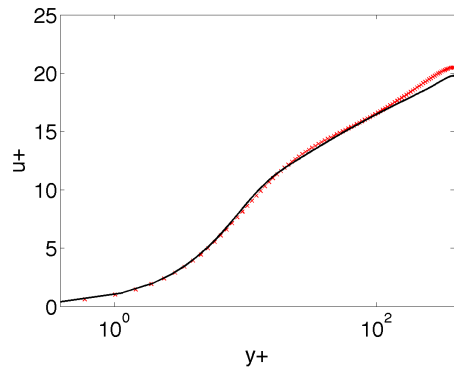
The ODT model parameters are $C = 6.5$ and $Z = 300$ which are the same as the ODTLES parameters in section 6.1 and 6.2. The maximum eddy length l^{max} is chosen to equal the channel half height h . The ODT resolution is $N_{\text{ODT}} = 1024$. To compute reliable ODT flow statistics a larger averaging period (or ensemble averaging) is required: the average time is $t_{\text{ave}} = 12800$ non-dimensional time units after reaching a steady state, which is significantly larger than $t_{\text{ave}} = 20$ in DNS.

Figure A.10 illustrates some representative results for ODT: The averaged streamwise velocity profile (see figure A.10a) and the overall turbulent kinetic energy (see figure A.10c–A.10e) are described very well within the ODT model including the full spectrum of the turbulent cascade. The similarity of ODT and DNS results implies a considerably small ODT model error σ_{ODT} . The ODT computing time is only ≈ 9 CPU-seconds to simulate for $t_{\text{ave}} = 20$ (the overall computing time is higher, because in the example the flow is averaged over $t_{\text{ave}} = 12800$). ODT is a convenient sub-grid model because of its low computational costs. Thereby ODT can compute a wide range of complex physical effects. In the turbulent channel case, ODT dynamically produces realistic wall profiles (see section 4.2). These properties outperform commonly used eddy viscosity models.

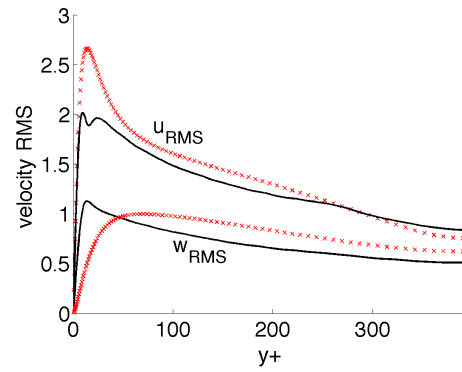
Further ODT results, including various physical small scale effects, are available in the literature (e.g. see Kerstein et al. (2001), Schmidt et al. (2013), Wunsch and Kerstein (2005), and Schulz et al. (2013)).

Appendix B. ODTLES: Numerical Implementation

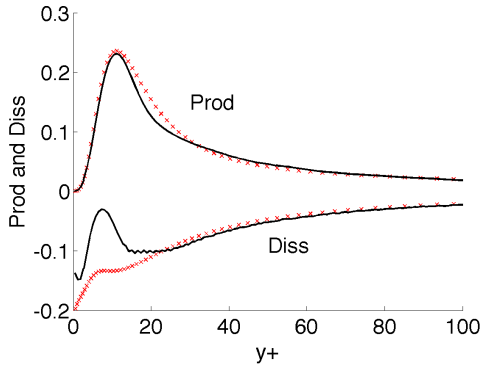
Table B.1 summarizes the numerical discretizations of the single fractional steps within the ODTLES advancement cycle (section 5). The ODT advancement (Eq. (39)) contains the XLES diffusion terms ($\underline{\mathcal{D}}_{\text{XLES}}$) treated as forcing terms for ODTLES.



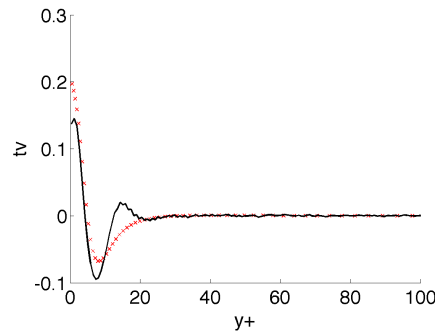
(a) ODT:
law of the wall.



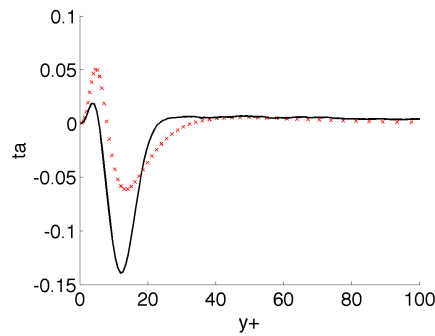
(b) Streamwise (u_{RMS}) and spanwise (w_{RMS}) velocity RMSs.



(c) Production (Prod) and Dissipation (Diss) of the turbulent kinetic energy.



(d) Viscous transport of the turbulent kinetic energy (tv).



(e) Advective transport of the turbulent kinetic energy (ta).

Figure A.10: Turbulent channel flow results ($Re_\tau = 395$) for DNS (small crosses) and ODT (solid) with $N_{ODT} = 1024$ cells.

Table B.1: Numerical Schemes:

In time: EE1 (1st order explicit Euler), RK3 (3rd order Runge-Kutta), CN (2nd order Crank-Nicolson), IE1 (1st order implicit Euler).

In space: UP1 (1st order upwind), CDM (2nd order central difference method).

factional step	time scheme	spatial scheme
Eq. (36)	EE1	UP1
Eq. (37)	RK3-CN + RK3-RK3	CDM
Eq. (38)	EE1	CDM
Eq. (39)	IE1 + triplet map + EE1	CDM
Eq. (40)	EE1	CDM

The coupled advection schemes RK3-CN-CDM and RK3-RK3-CDM are described and validated in part I (Glawe et al., 2015, section 3.3). All velocities are discretized using a staggered grid.

Ashurst, W. T., Kerstein, A. R., 2005. One-dimensional turbulence: Variable-density formulation and application to mixing layers. *Phys. Fluids* 17, 025107.

Cao, S., Echehki, T., 2008. A low-dimensional stochastic closure model for combustion large-eddy simulation. *J. Turbul.* 9, 1–35.

Chapman, D. R., 1979. Computational aerodynamics development and outlook 17, 1293–1313.

Choi, H., Moin, P., 2012. Grid-point requirements for large eddy simulation: Chapman's estimates revisited. *Phys. Fluids* 24, 31–36.

Cline, D. A., 2015. A novel modeling approach for multiscale, multiphysics flow. Poster presented at SIAM CSE15, March 14–18, 2015, Salt Lake City, USA.

Ferziger, J., Peric, M., 1999. *Computational Methods for Fluid Dynamics*. Springer.

Germano, M., Piomelli, U., Moin, P., Cabot, W. H., 1991. A dynamic subgrid-scale eddy viscosity model. *Phys. Fluids A: Fluid Dynamics* 3, 1760–1765.

- Glawe, C., Schmidt, H., Kerstein, A., Klein, R., 2015. XLES part I: Introduction to extended large eddy simulation. submitted to *J. Comput. Phys.*
- Glawe, C., Schulz, F., Gonzalez-Juez, E., Schmidt, H., Kerstein, A., 2013. ODTLES simulations of turbulent flows through heated channels and ducts. In: *Proceedings of TSFP-8*. Poitiers, France.
- Gonzalez-Juez, E. D., Schmidt, R. C., Kerstein, A. R., 2011. ODTLES simulation of wall-bounded turbulent flows. *Phys. Fluids* 23, 125102.
- Kawamura, H., Dec. 2014. DNS database. <http://murasun.me.noda.tus.ac.jp/turbulence/index.html>, [Online; accessed Dec 2014].
- Kawamura, H., Abe, H., Matsuo, Y., 1999. DNS of turbulent heat transfer in channel flow with respect to Reynolds and Prandtl number effects. *Int. J. Heat Fluid Fl.* 20, 196–207.
- Kerstein, A. R., 1999. One-dimensional turbulence: Model formulation and application to homogeneous turbulence, shear flows, and buoyant stratified flows. *J. Fluid Mech.* 392, 277–334.
- Kerstein, A. R., Ashurst, W. T., Wunsch, S., Nilsen, V., 2001. One-dimensional turbulence: Vector formulation and application to free shear flows. *J. Fluid Mech.* 447, 85–109.
- Lee, M., Malaya, N., Moser, R. D., 2013. Petascale direct numerical simulation of turbulent channel flow on up to 786k cores. In: *Proceedings of SC13: International Conference on High Performance Computing, Networking, Storage and Analysis*. ACM, pp. 1–11.
- Lee, M., Moser, R. D., 2014a. Direct numerical simulation of turbulent channel flow up to $Re_\tau = 5200$. under consideration for publication in *J. Fluid Mech.*
- Lee, M., Moser, R. D., Dec. 2014b. DNS database. <http://turbulence.ices.utexas.edu>, [Online; accessed Feb 2015].
- Lignell, D., Kerstein, A., Sun, G., Monson, E. I., 2013. Mesh adaption for efficient multiscale implementation of one-dimensional turbulence. *Theor. Comput. Fluid Dyn.* 27, 273–295.

- Meiselbach, F. T., Apr 2015a. private communication.
- Meiselbach, F. T., 2015b. Application of ODT to turbulent flow problems. Ph.D. thesis.
- Menon, S., Kerstein, A., 2011. The linear-eddy model. In: Echehki, T., Mastorakos, E. (Eds.), *Turbulent Combustion Modeling: Advances, New Trends and Perspectives*. Springer, pp. 221–247.
- Pinelli, A., Uhlmann, M., Sekimoto, A., Kawahara, G., 2010. Reynolds number dependence of mean flow structure in square duct turbulence. *J. Fluid Mech.* 644, 107–122.
- Pope, S., 2000. *Turbulent Flows*. Cambridge University Press.
- Sagaut, P., 2006. *Large Eddy Simulation for Incompressible Flows: An Introduction*. Springer Verlag.
- Sannan, S., Weydahl, T., Kerstein, A. R., 2013. Stochastic simulation of scalar mixing capturing unsteadiness and small-scale structure based on mean-flow properties. *Flow Turbul. Combust.* 90, 189–216.
- Schlatter, P., Örlü, R., 2010. Assessment of direct numerical simulation data of turbulent boundary layers. *J. Fluid Mech.* 659, 116–126.
- Schmidt, H., Kerstein, A. R., Wunsch, S., Nédélec, R., Sayler, B. J., 2013. Analysis and numerical simulation of a laboratory analog of radiatively induced cloud-top entrainment. *Theor. Comp. Fluid Dyn.* 27, 377–395.
- Schmidt, R. C., Kerstein, A. R., McDermott, R., 2008. ODTLES: A multi-scale model for 3D turbulent flow based on one-dimensional turbulence modeling. *Comput. Methods Appl. Mech. Engrg.* 199, 865–880.
- Schulz, F., Glawe, C., Schmidt, H., Kerstein, A., 2013. Toward modeling of CO₂ multi-phase flow patterns using a stochastic multi-scale approach. *Environmental Earth Sciences* 70, 3739–3748.
- Uhlmann, M., Feb. 2013. DNS database. `\protect\protect\protect\edefOT1{OT1}\let\enc@update\relax\protect\edefcmr{cmr}\protect\edefm{m}\protect\edefn{n}\protect\xdef\OT1/cmr/m/n/12{\OT1/cmr/m/n/12}\OT1/cmr/m/n/12\size@update\enc@`

`update\ignorespaces\relax\protect\relax\protect\edef\cmr{cmr}\protect\xdef\OT1/cmr/m/n/12{\OT1/cmr/m/n/12}\OT1/cmr/m/n/12\size@update\enc@updatewww.ifh.kit.edu/dns_data$, [Online; accessed Feb 2013].`

Uhlmann, M., Pinelli, A., Kawahara, G., Sekimoto, A., 2007. Marginally turbulent flow in a square duct. *J. Fluid Mech.* 588, 153–162.

Wunsch, S., Kerstein, A. R., 2005. A stochastic model for high-Rayleigh-number convection. *J. Fluid Mech.* 528, 173–205.